Combined Role of High- and Low-Frequency Processes of Equatorial Zonal Transport in Terminating an ENSO Event

HAN-CHING CHEN AND CHUNG-HSIUNG SUI

Department of Atmospheric Sciences, National Taiwan University, Taipei, Taiwan

YU-HENG TSENG

Institute of Oceanography, National Taiwan University, Taipei, Taiwan

BOHUA HUANG

Department of Atmospheric, Oceanic and Earth Sciences, College of Science, George Mason University, Fairfax, Virginia

(Manuscript received 18 May 2017, in final form 23 March 2018)

ABSTRACT

This study investigates the sudden reversal of anomalous zonal equatorial transport above thermocline at the peak phase of ENSO. The oceanic processes associated with zonal transport are separated into low-frequency ENSO cycle and high-frequency oceanic wave processes. Both processes can generate a reversal of equatorial zonal current at the ENSO peak phase, which is a trigger for the rapid termination of ENSO events. For the low-frequency process, zonal transport exhibits slower and basinwide evolution. During the developing phase of El Niño (La Niña), eastward (westward) transport prevails in the central-eastern Pacific, which enhances ENSO. At the peak of ENSO, a basinwide reversal of the zonal transport resulting from the recharge–discharge process occurs and weakens the existing SST anomalies. High-frequency zonal transport presents clear eastward propagation related to Kelvin wave propagation at the equator, reflection at the eastern boundary, and the westward propagating Rossby waves. The major westerly wind bursts (easterly wind surges) occur in late boreal summer and fall with coincident downwelling (upwelling) Kelvin waves for El Niño (La Niña) events. After the peak of El Niño (La Niña), Kelvin waves reach the eastern boundary in boreal winter and reflect as off-equatorial Rossby waves; then, the zonal transport switches from eastward (westward) to westward (eastward). The high-frequency zonal transport can be represented by equatorial wave dynamics captured by the first three EOFs based on the high-pass-filtered equatorial thermocline. The transport anomaly during the decaying phase is dominated by the low-frequency process in El Niño. However, the transport anomaly is caused by both low- and high-frequency processes during La Niña.

1. Introduction

The El Niño–Southern Oscillation (ENSO) phenomenon is the dominant phenomenon of interannual climate variability in the tropical ocean–atmosphere system in the Pacific, having great impact on global weather and climate. The onset of ENSO events generally occurs during boreal spring and summer, while peak amplitudes in the sea surface temperature (SST) anomalies are usually attained during boreal winter, with the amplitudes decaying in the next spring. The positive dynamical feedback mechanism, known as the Bjerknes feedback, can magnify and maintain the SST anomalies (Bjerknes 1969). On the other hand, the phase transition of ENSO events requires a delayed negative feedback that eliminates the original SST anomalies. The ''recharge–discharge oscillator'' postulates that the establishment of warm water volume (WWV) can facilitate the phase transition of ENSO events (Jin 1997a,b; Li 1997).

Although the recharge–discharge oscillator could explain how the coupled ocean–atmosphere system oscillates, the gradual phase transition within a low-frequency ENSO cycle could not adequately explain the more sudden termination of an ENSO event, compared with its growth. Chen et al. (2016) showed that the

Corresponding author: Dr. Chung-Hsiung Sui, sui@as.ntu.edu.tw

DOI: 10.1175/JCLI-D-17-0329.1

© 2018 American Meteorological Society. For information regarding reuse of this content and general copyright information, consult the AMS Copyright Policy (www.ametsoc.org/PUBSReuseLicenses).

abrupt basinwide reversal of the equatorial zonal transport anomaly above the depth of the 20°C isotherm (D20) at the peak phase of SST anomalies is a trigger for the rapid termination of ENSO. Chen et al. (2016) demonstrated that the equatorial zonal transport anomaly is dominated by the meridional structure of the thermocline anomaly on and off the equator. The reversal of zonal transport weakens the ENSO SST anomalies through reversed advection and reduces the existing zonal tilting anomalies of the equatorial thermocline. Those processes help control the ocean at the peak phase of ENSO during the evolution of both El Niño and La Niña.

Although ENSO exists largely on interannual time scales through interactions between oceanic and atmospheric dynamics (Bjerknes 1969; Battisti 1988; Schopf and Suarez 1988; Kessler 2002), it strongly modulates and responds to the high-frequency variability. Previous studies have suggested that the ENSO cycle exists due to a combination of high-frequency ocean wave dynamics and an amplification by coupled ocean–atmosphere interactions (Philander 1983; Hirst 1986). The high-frequency oceanic Kelvin waves might influence the evolution of the ENSO by moving warm or cold water eastward (Harrison and Schopf 1984; Fedorov and Melville 2000; Roundy and Kiladis 2006). The high-frequency eastward-propagating equatorial Kelvin waves can be excited by the westerly wind bursts (WWBs; e.g., McPhaden and Yu 1999; Delcroix et al. 2000; Kessler 2002; Roundy and Kiladis 2006; Fedorov et al. 2015). The WWBs are commonly associated with the onset and growth of El Niño events (McPhaden 2004), while the easterly wind surges (EWSs) play an important role in the onset and maintaining phase of La Niña (Chiodi and Harrison 2015). Thus, it is important to investigate how the downwelling (upwelling) oceanic Kelvin waves are generated by WWBs (EWSs) in boreal summer and fall, and reach the eastern boundary in boreal winter for El Niño (La Niña) events.

The ENSO events are dominated primarily by the large-scale air–sea interaction. However, challenges still remain to explain the comprehensive aspects of ENSO, especially the vastly varying temporal characteristics and amplitudes among individual ENSO events. The main objective of this manuscript is to show the impact of high-frequency atmospheric and oceanic variations on the ENSO evolution and explain how they vary among different ENSO events. We demonstrate that the oceanic processes discussed in Chen et al. (2016) can be separated into the low-frequency ENSO cycle and high-frequency oceanic wave process. The low-frequency ENSO cycle includes an east–west thermocline-tilting mode and a recharge–discharge mode (Li 1997; Jin 1997a), and the high-frequency process represents the characteristics of wave dynamics, which include the propagation and reflection of Rossby and Kelvin waves (Suarez and Schopf 1988; Battisti and Hirst 1989; Picaut et al. 1997).

The rest of the paper is structured as follows. Section 2 describes the datasets and the methods used in this paper. Section 3a describes the general characteristics of the high- and low-frequency equatorial zonal transport above the thermocline in El Niño and La Niña events, using 15-month low-pass and high-pass filters. Section 3b discusses the roles of the low-frequency process played by both the east–west thermocline-tilting mode and recharge–discharge mode, as well as the physical processes that generate these anomalous currents. Section 3c focuses on the contributions of the wave dynamics in the high-frequency process to the zonal current. Finally, a discussion and summary are presented in section 4 and 5, respectively.

2. Data and method

The pentad D20 and the ocean current are obtained from the Global Ocean Data Assimilation System (GODAS) on a 0.333° latitude × 1.0° longitude global grid (Behringer and Xue 2004). D20 is generally used as an indicator for the tropical thermocline depth. Therefore, the ocean mass transport above the thermocline is defined in this study as transport vertically integrated from the surface to D20. The pentad-averaged near-surface wind data (0.995 sigma level) from NCEP–NCAR Reanalysis 1 (Kalnay et al. 1996) on a 2° × 2° grid is used to analyze the corresponding ocean–atmosphere interactions. The SST dataset used in this study is the NOAA 1/4° daily Optimum Interpolation Sea Surface Temperature (OISST; Reynolds et al. 2007).

The selection of ENSO events follows the ENSO year definition by the Climate Prediction Center of NOAA based on a monthly Niño-3.4 index (http://www.cpc.ncep.noaa.gov/products/analysis_monitoring/ensostuff/ensoyears.shtml) from 1980 to 2017. Only moderate and strong El Niño and La Niña events with five consecutive overlapping 3-month mean Niño-3.4 SST anomalies at or above 1.0°C are used in the composite analysis of this study. We exclude the event in 1987/88 because this event followed a strong El Niño and did not reach its peak intensity near boreal winter. During the analysis period, there were six El Niño events (1982/83, 1986/87, 1991/92, 1997/98, 2002/03, and 2009/10) and five La Niña events (1988/89, 1998/99, 1999/00, 2007/08, and 2010/11) in which composites were calculated. A composite El Niño (La Niña) event is defined as the average of the corresponding calendar months of all El Niño (La Niña) events over a maximum of three years, starting from

the developing year [Year(0)] to the decaying year [Year(1)] and afterward [Year(2)]. Independently, the 2015/16 El Niño event is discussed in section 4.

The major part of the anomalous zonal transport on the ENSO time scale is found to be associated with an anomalous zonal geostrophic current. In the equatorial waveguide, the geostrophic balance is a very good approximation for the momentum balance in the meridional direction. Because the equatorial zonal transport anomaly is predominantly geostrophic (Chen et al. 2016), an E index based on the geostrophic balance is defined to examine the transport. The geostrophic balance links the zonal velocity at the equator to the second derivative of D20 with respect to latitude as

$$\beta u_{\mathrm{EQ}} \approx -g' \frac{\partial^2(\mathrm{D20})}{\partial y^2}, \tag{1}$$

where $\beta = 2\Omega/R$, subscript EQ is defined as 0° latitude, and g' is the reduced gravity. In finite differencing format, $-\partial^2(\mathrm{D20})/\partial y^2$ is proportional to

$$\begin{aligned} E &= -[(\mathrm{D20}_{5^\circ\mathrm{N}} - \mathrm{D20}_{\mathrm{EQ}}) - (\mathrm{D20}_{\mathrm{EQ}} - \mathrm{D20}_{5^\circ\mathrm{S}})] \\ &= 2 \times \mathrm{D20}_{\mathrm{EQ}} - \mathrm{D20}_{5^\circ\mathrm{N}} - \mathrm{D20}_{5^\circ\mathrm{S}}. \end{aligned} \tag{2}$$

Assuming that the D20 anomaly is symmetric to the equator, E measures the relative magnitude of the $\mathrm{D20}_{\mathrm{EQ}}$ anomaly with respect to the off-equatorial ones ($\mathrm{D20}_{5^\circ\mathrm{N}}$ and $\mathrm{D20}_{5^\circ\mathrm{S}}$). When E is positive, D20 concaves up at the equator and the geostrophic zonal transport is eastward. Similarly, when E is negative or the D20 anomaly concaves down at the equator, there is a westward geostrophic zonal transport anomaly.

3. Results

a. General features of El Niño and La Niña

The composite evolution of the sea surface temperature anomalies (shading) and zonal surface wind anomalies (contours) for the El Niño and La Niña events, used to investigate the life cycle of ENSO events, are presented in Fig. 1. The peaks of westerly (easterly) wind anomalies are collocated with minimum (maximum) zonal gradients of SST anomalies, suggesting that SST and near-surface wind anomalies are amplified through the Bjerknes feedback at the equator (Bjerknes 1969). During the developing phase, the zonal wind anomalies migrate eastward from Jun(0) to Apr(1) for the El Niño events (contour, Fig. 1a), while the wind anomalies remain stationary during the same period for the La Niña events (contour, Fig. 1b). During the decaying phase, the negative SST anomalies for the El Niño events start to propagate eastward in May(1), and the El Niño events are ended as the cold SST anomalies move into the central Pacific during the summer of Year(1). However, for the La Niña events, the positive SST anomalies remain stationary in the western equatorial Pacific (west of 150°E) without any propagation (shading, Fig. 1b). It is interesting to note that the rapid westward decay of the SST anomalies occurs in the eastern Pacific (east of 120°W) after the peak of the event in both the El Niño and La Niña cases. On the other hand, the SST anomalies in the central Pacific (150°W to the date line), which are in balance with the zonal wind anomalies, are much more persistent after the peak of ENSO (Fig. 1). The rapid decay of the ENSO events from Jan(1) to Apr(1) after the maturing phase leads to the termination of an El Niño and the significant weakening of a La Niña (Chen et al. 2016).

The fast decay of SST anomalies after the maturing phase is closely connected to the reversal of zonal transport in the eastern Pacific (Chen et al. 2016). To investigate the evolution of the equatorial zonal transport above the thermocline and the meridional concavity of the thermocline, the composite evolution of the equatorial zonal transport above the thermocline (contours) and E (shading) for the El Niño and La Niña events are presented in Fig. 2. The zonal transport anomaly above D20 corresponds well with the E anomaly during the entire ENSO life cycle, confirming that the equatorial zonal current is mainly dominated by the meridional thermocline structure, through the geostrophic balance (Chen et al. 2016; Jin and An 1999). Two episodes of eastward (westward) transport prevail in the central and eastern Pacific during the development of El Niño (La Niña) [Year(0)], one from Mar(0) to Jun(0) and the other from Aug(0) to Nov(0), with a break in Jul(0). During these two episodes, the zonal transport is controlled by the equatorial thermocline ($\mathrm{D20}_{\mathrm{EQ}}$) while enhancing the thermocline feedback, as suggested by An and Jin (2001). The first reversed zonal transport anomaly driven by local D20 anomalies at the equator appears during Oct(0)–Nov(0) between 150°E and the date line. For El Niño events, the initial reversed zonal transport anomaly is mainly driven by the equatorial thermocline anomaly, which is associated with local zonal wind stress (Chen et al. 2016). The reversal of the zonal transport anomaly first appears in the longitude band from 150°E to the date line where the surface westerly wind stress is largest (contour, Fig. 1a). As a result, the strong meridional discharge of water mass causes substantial shoaling of the thermocline, making the equatorial thermocline anomaly shallower than the off-equatorial ones. A similar situation occurs in the La Niña events in opposite sign to the El Niño events. After the mature phase of ENSO, the off-equatorial thermocline

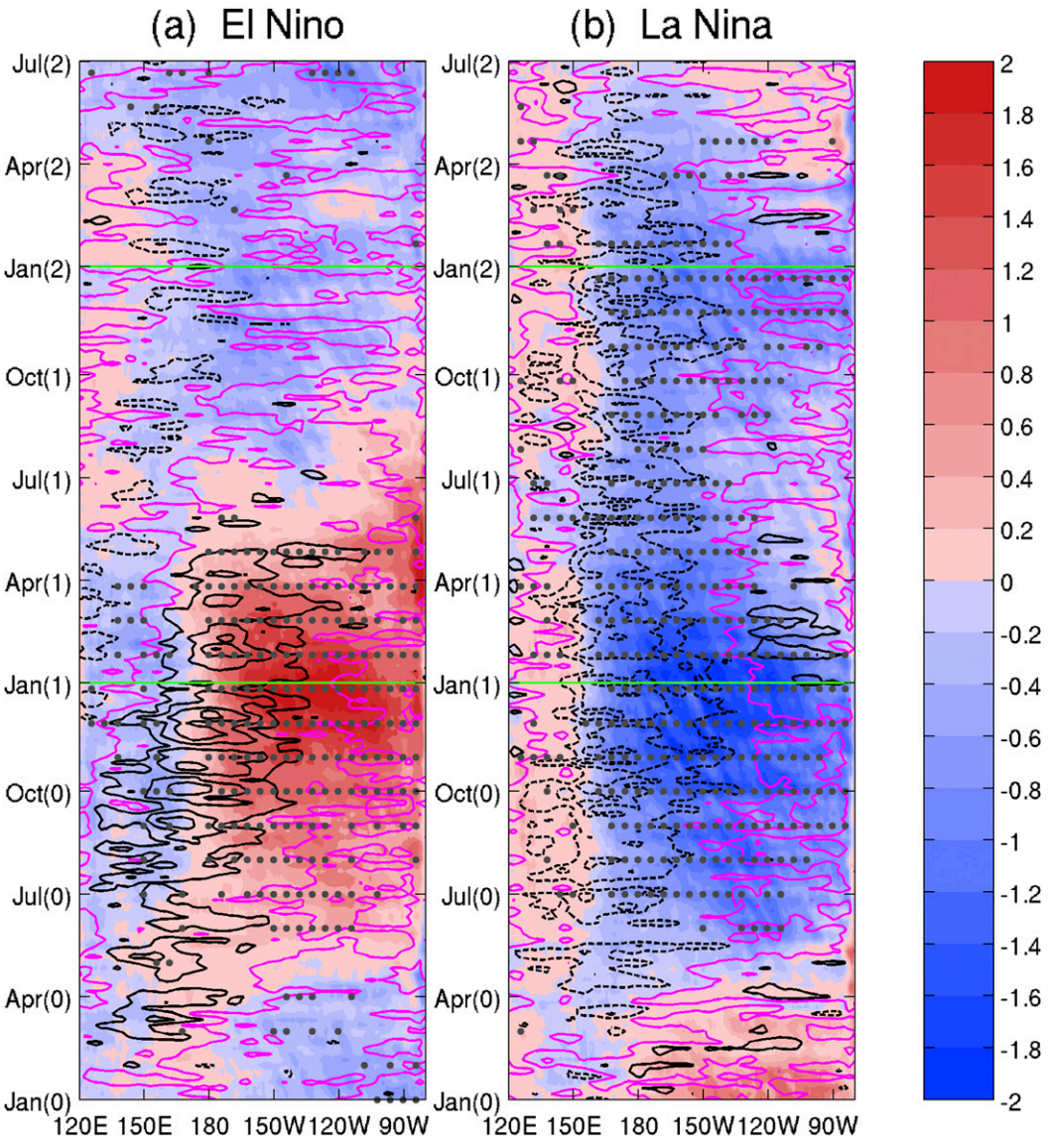

FIG. 1. Hovmöller diagram of SST anomalies (color shading) and surface zonal wind anomalies (contours) averaged between 5°S and 5°N for composites of (a) El Niño and (b) La Niña years. The purple lines represent zero values and solid (dashed) lines indicate positive (negative) wind anomalies. The contour interval is 1 m s^{-1} for wind anomalies and the shading interval is 0.2°C for SST anomalies. The black dots indicate the composite of SST anomalies exceeding a 90% confidence level using a *t* test The green lines represent January of Year(1) [Jan(0)] and Year(2) [Jan(2)], respectively.

depth anomaly become more important. This change in concavity of the thermocline anomalies, induced by the recharge–discharge process associated with local wind forcing and the reflected Rossby waves off the equator, reverses the zonal transport anomalies rapidly in the entire Pacific basin, forming a basinwide transport reversal (shading, Fig. 2).

Figure 3 shows the power spectrum analysis of zonal transport anomalies averaged over the equatorial eastern Pacific region (5°S–5°N, 160°W–80°W). It is worth noting that the zonal transport anomalies include two major processes with different time scales. The time scale of the slower process is dominated by strong interannual variability with periods varying from 15 months to 6 years. The other process exhibits a higher frequency with a period of less than one year. To identify these two major processes, 15-month low-pass and high-pass filters are used to separate the high-frequency and low-frequency processes. After the 15-month low-pass and high-pass filters are performed, the composites are calculated to show the

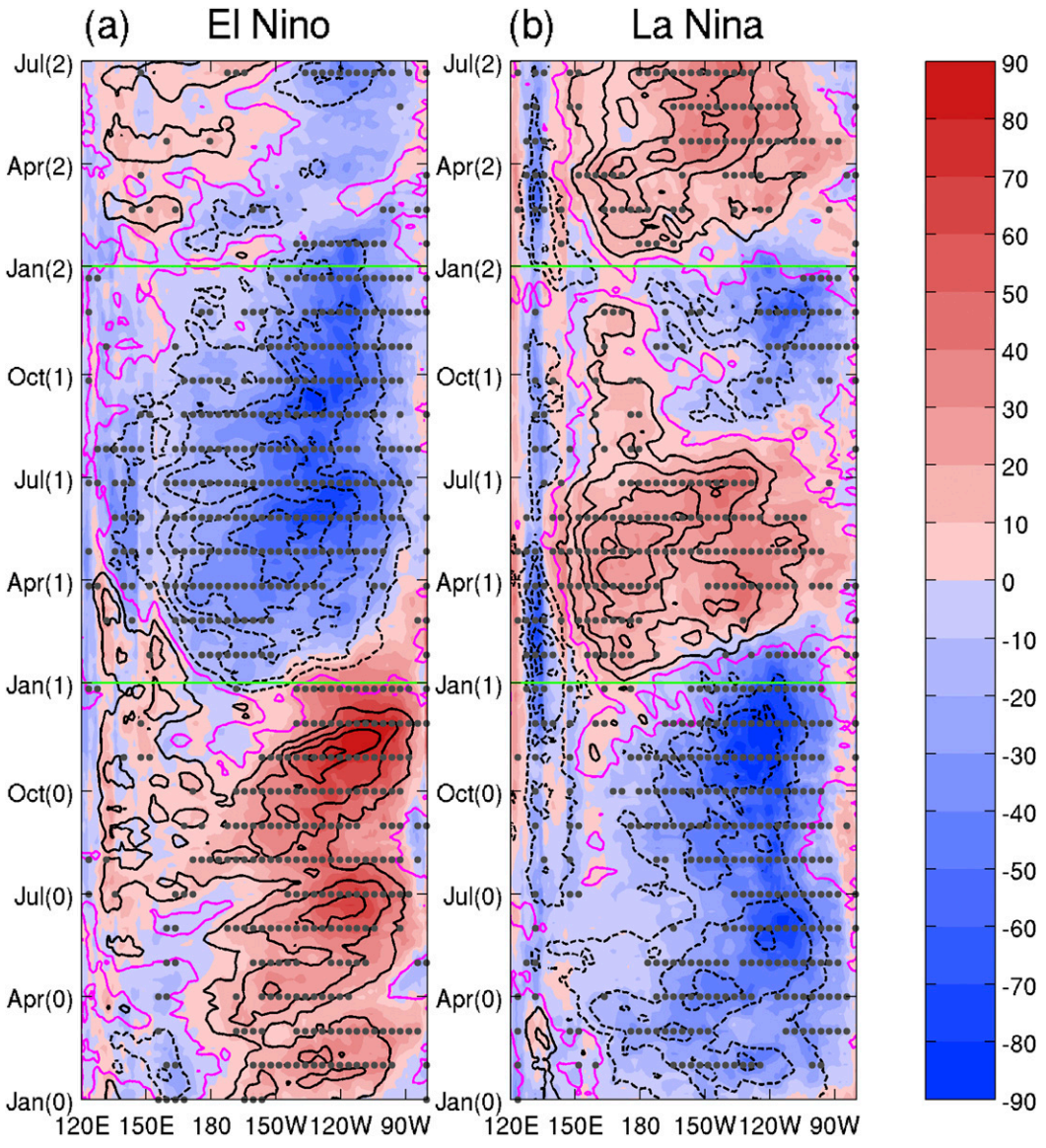

FIG. 2. As in Fig. 1, but for E anomalies (color shading) and zonal transport anomalies (contours). The quantity E measures the relative magnitude of the $D20_{EQ}$ anomaly with respect to the off-equatorial ones ($D20_{5°N}$ and $D20_{5°}$). The contour interval is 0.3 Sv for transport anomalies and the shading interval is 10 m for E anomalies.

composite evolution of the E anomalies (shading) and zonal transport anomalies (contours) along the equator during El Niño and La Niña (Fig. 4). The low-frequency process exhibits a slower and more basinwide evolution (Figs. 4a,b), which is associated with the recharge–discharge process. During the developing phase of El Niño (La Niña), the eastward (westward) transport prevails in the central and eastern Pacific (east of the date line). In Oct(0)–Nov(0), the gradual reversal of the zonal transport anomaly emerges near the date line. After that, a basinwide reversal of transport and E anomalies occurs around Jan(1). Compared to the low-frequency process, the high-frequency process exhibits significant eastward propagation (Figs. 4c,d). During the first year [Year(0)], a series of eastward-moving disturbances consisting of eastward transport and westward transport appears to be related to the Kelvin waves at the equator. After the peak of El Niño (La Niña), the high-frequency zonal transport suddenly switches from eastward (westward) to westward (eastward), which is caused by the wave reflection at the eastern boundary. Details of the dynamic processes of zonal transport will be discussed in later sections.

The zonal transport anomalies and SST anomalies averaged over the equatorial eastern Pacific region

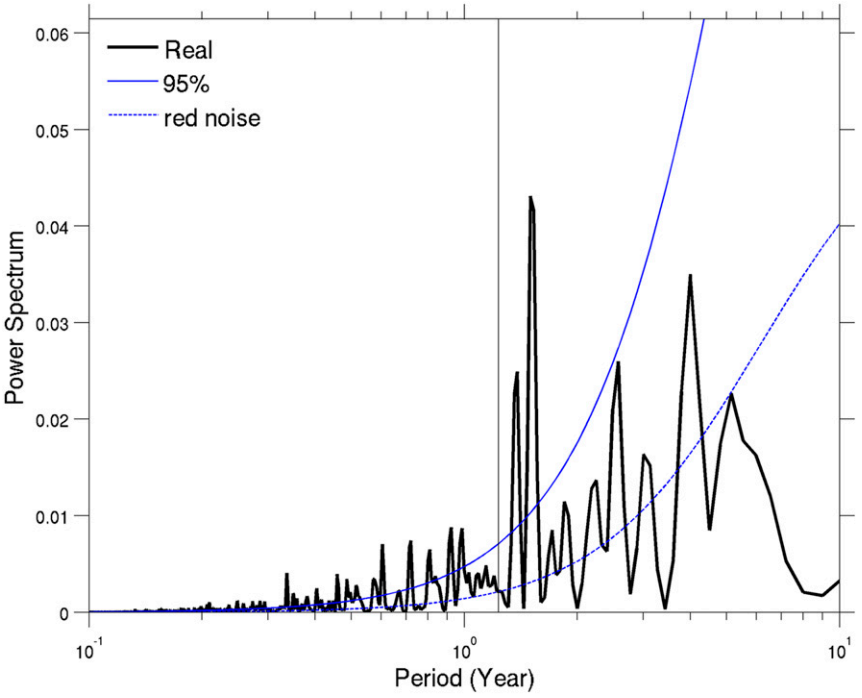

FIG. 3. Power spectrum analysis of zonal transport anomalies averaged over the equatorial eastern Pacific region (5°S–5°N, 160°–80°W). Red noise (lower and dashed blue curve) and the 95% statistical confidence (upper and solid blue curve) are indicated. The vertical gray line represents a period of 15 months.

(5°S–5°N, 160°W–80°W), used to assess the contribution of low-frequency and high-frequency processes and the relationship between zonal transport and SST evolution, are shown in Fig. 5. During the developing phase [Year(0)], the magnitude of the unfiltered zonal transport anomaly (gray area) is dominated by the low-frequency transport anomaly (red curves). However, the high-pass-filtered transport (blue curves) results in the fluctuation of the unfiltered zonal transport anomaly. The fluctuation of high-pass-filtered transport corresponds to the two episodes of the eastward (westward) wave propagation in the central and eastern Pacific (Figs. 5c,d). These signals correspond to the zonal temperature advection described in Picaut et al. (1997), which enhances the thermocline feedback during ENSO development, as suggested by An and Jin (2001).

During the transition phase, the low-frequency and high-frequency processes both seem to play important roles in the phase transition at the peak phase of ENSO. The reversals of low-pass and high-pass-filtered transport anomalies both appear in boreal winter. The transition from warming to cooling (cooling to warming) in El Niño (La Niña) events due to the low-pass-filtered transport anomaly occurs slightly earlier than that due to the high-pass-filtered transport anomaly. It is noted that the reversals of the high-frequency transport are more rapid than those of low-frequency transport.

After the mature phase [Year(1)], the reversed zonal transport anomaly quickly weakens the thermocline feedback and advection feedback associated with SST anomalies in the eastern Pacific (Jin and An 1999). For El Niño events, the transport anomaly during the decaying phase is more dominated by the low-frequency process; however, the transport anomaly is caused by both low- and high-frequency processes during the decaying phase of La Niña. The difference in the contribution to the transport between El Niño and La Niña is due to the asymmetry of evolution in the low-frequency process (Figs. 4a,b). During the developing phase in El Niño and La Niña events, the major low-frequency processes of zonal transport occur in the central-eastern Pacific. During the decaying phase, for El Niño, the processes of transport are still located in the central-eastern Pacific after the transport is reversed; however, for La Niña, the center of reversed transport shifts to the western Pacific because of the stationary local wind-forcing (contour, Fig. 1b). Consequently, the magnitude of low-frequency zonal transport anomaly over the eastern Pacific (red curves, Fig. 5) during the decaying phase is larger in El Niño events than in

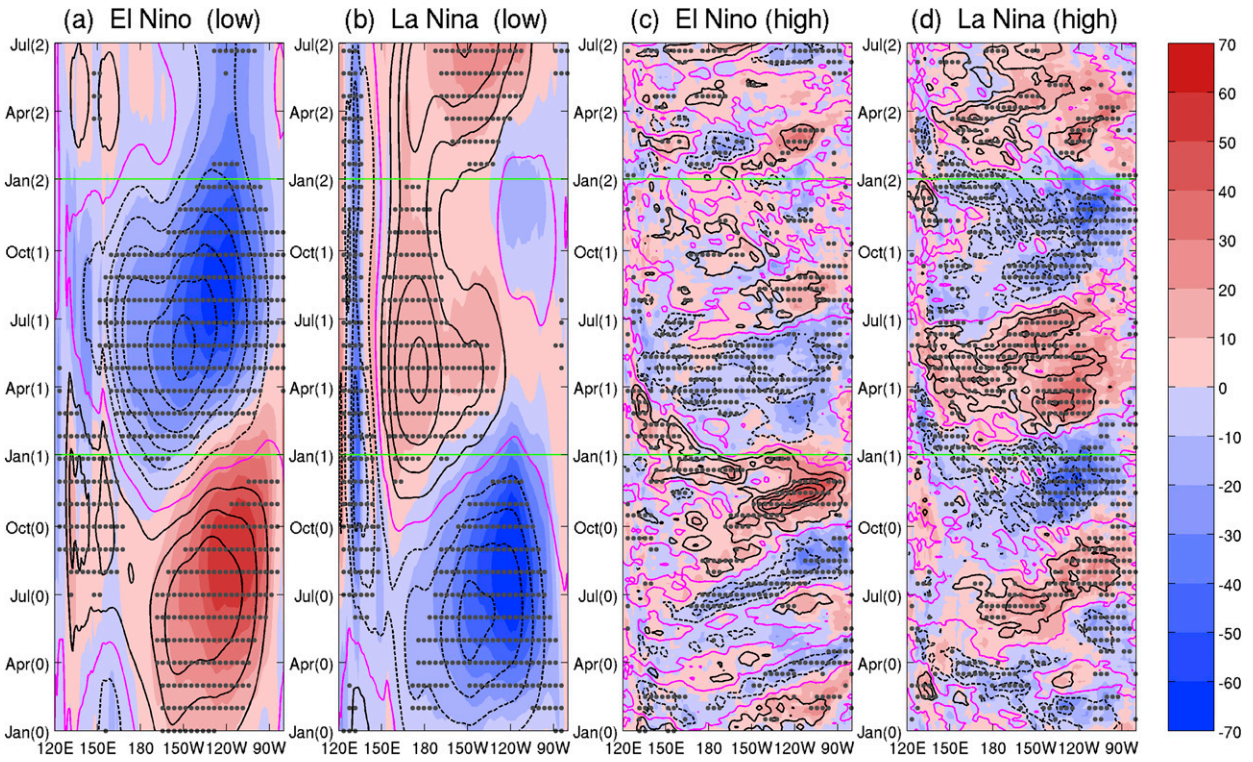

FIG. 4. Hovmöller diagram of E anomalies (color shading) and zonal transport anomalies (contours) averaged between 5°S and 5°N with a 15-month (a),(b) low-pass and (c),(d) high-pass filter for composite of (a),(c) El Niño and (b),(d) La Niña years; E measures the relative magnitude of the $D20_{EQ}$ anomaly with respect to the off-equatorial ones ($D20_{5°N}$ and $D20_{5°S}$). The purple lines represent zero transport and solid (dashed) lines for positive (negative) transport anomalies. The black dots indicate the composite of transport anomalies exceeding a 90% confidence level using a t test. The contour interval is 0.2 Sv for transport anomalies and the shading interval is 10 m for E anomalies. The green lines represent Jan(1) and Jan(2), respectively.

La Niña events, resulting in the dominant contribution of the low-frequency process to the zonal transport anomaly in El Niño events.

b. *Low-frequency process*

On the ENSO time scale, the leading ocean dynamical modes are the east–west tilting mode and recharge–discharge mode (Li 1997; Jin 1997a). To analyze the structure of the variations in the thermocline over time, an empirical orthogonal function (EOF) analysis (Emery and Thomson 2001) was performed on the 15-month low-pass-filtered D20 in the equatorial region (10°S–10°N, 120°E–80°W). These two modes represent 45.8% and 25.6%, respectively, of the total variance in D20 (not shown). The first mode can be viewed as an east–west tilting mode with the axis near 160°W, and the second mode involves more of a north–south oscillation, called the recharge–discharge mode, with a maximum variance around 150°W at the equator. The maximum correlation between the two modes occurs with the recharge–discharge mode leading the tilting mode by about 8.2 months. The phase delay is consistent with the phase lag between the zonal-mean thermocline depth anomaly and the SST anomaly, as described by Li (1997), based on the proportional relationship between the change in the zonal-mean thermocline and the zonal-mean wind stress.

We reconstruct the thermocline field based on EOFs to investigate the contribution of these two modes to the meridional structure of the equatorial thermocline related to the geostrophic balance (i.e., the E index defined in section 2). The reconstructed E anomalies, which are based on the first two EOF modes of the low-frequency process, are plotted in Fig. 6 to show the contribution of these two modes. The shadings in Fig. 6 indicate that low-pass-filtered E anomalies and contours represent the reconstructed E anomalies based on EOF1, EOF2, and EOF1 + EOF2. The first two EOFs (contour, Figs. 6a,d) provide a good overall fit to the low-frequency process (shading, Figs. 6a,d), indicating that the east–west tilting and recharge–discharge mode can determine the evolution of the equatorial thermocline. On the other hand, this relationship holds better for El Niño than for the La Niña cases. For instance, the

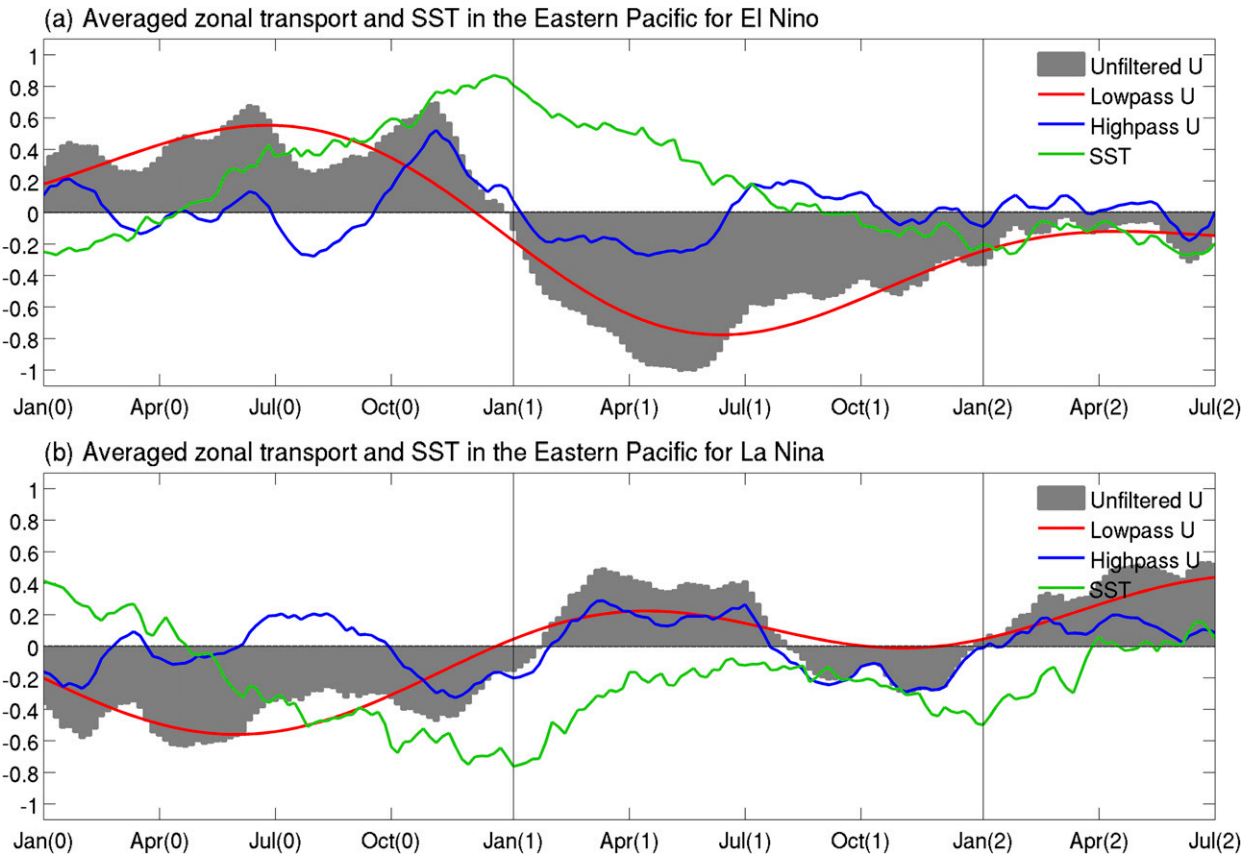

FIG. 5. Zonal transport anomalies (Sv) and SST anomalies (green curves; scaled by 2°C) averaged over the equatorial eastern Pacific region (5°S–5°N, 160°–80°W) for (a) El Niño and (b) La Niña years. The gray areas represent the unfiltered transport anomalies. The red (blue) curves represent the zonal transport anomalies with a 15-month low- (high-) pass filter.

E anomalies are well represented by the EOF1 + EOF2 in the El Niño cases (Fig. 6a) during the entire period but cannot be captured in the La Niña cases (Fig. 6d), particularly after the peak phase. The missing EOF2 signals in the La Niña cases after the peak phase (Fig. 6f), found in such characteristics as the surface wind and SST anomalies, are due to the asymmetric pattern of La Niña but cannot be well represented by EOF analysis.

The tilting mode (contours, Figs. 6b,e) represents the longitudinal slope of the equatorial thermocline depth anomalies (Li 1997; Jin 1997a). In the tilting process, the SST and surface wind are in phase with the zonally asymmetric thermocline depth anomaly related to the positive feedback process (Bjerknes feedback). In the El Niño cases (Fig. 6b), the tilting mode corresponds to the eastward transport from Jul(0) to Jul(1), peaking at Jan(1). This is apparently due to the deepened thermocline depth in the eastern equatorial Pacific. In the La Niña cases, the westward transport induced by the tilting mode also peaks in Jan(1); however, it lingers until the following year Jan(2). Overall, the tilting mode does not contribute to the reversal of the zonal current in Jan(1). As a result, the east–west tilting process could only change the zonal structure of thermocline anomalies; the tilting mode has little impact on zonal geostrophic transport (Jin and An 1999). On the other hand, the recharge–discharge mode involves a negative feedback between the zonal-mean thermocline depth anomaly and the wind anomaly, while the zonal-mean thermocline depth anomaly is not in equilibrium with the surface wind (Li 1997; Jin 1997a). The recharge–discharge process could change the meridional structure of thermocline anomalies via Sverdrup transport, so the recharge–discharge mode is significant in determining the zonal geostrophic transport. In fact, the reversal of the zonal transport occurs in Jan(1), suggesting that the phase transition is mainly determined by the recharge–discharge mode (contours, Figs. 6c,f). The maximum amplitude of *E* anomalies associated with EOF2 is located around 120°W in both El Niño and La Niña events. The EOF2 (contours, Figs. 6c,f) switches its phase at the

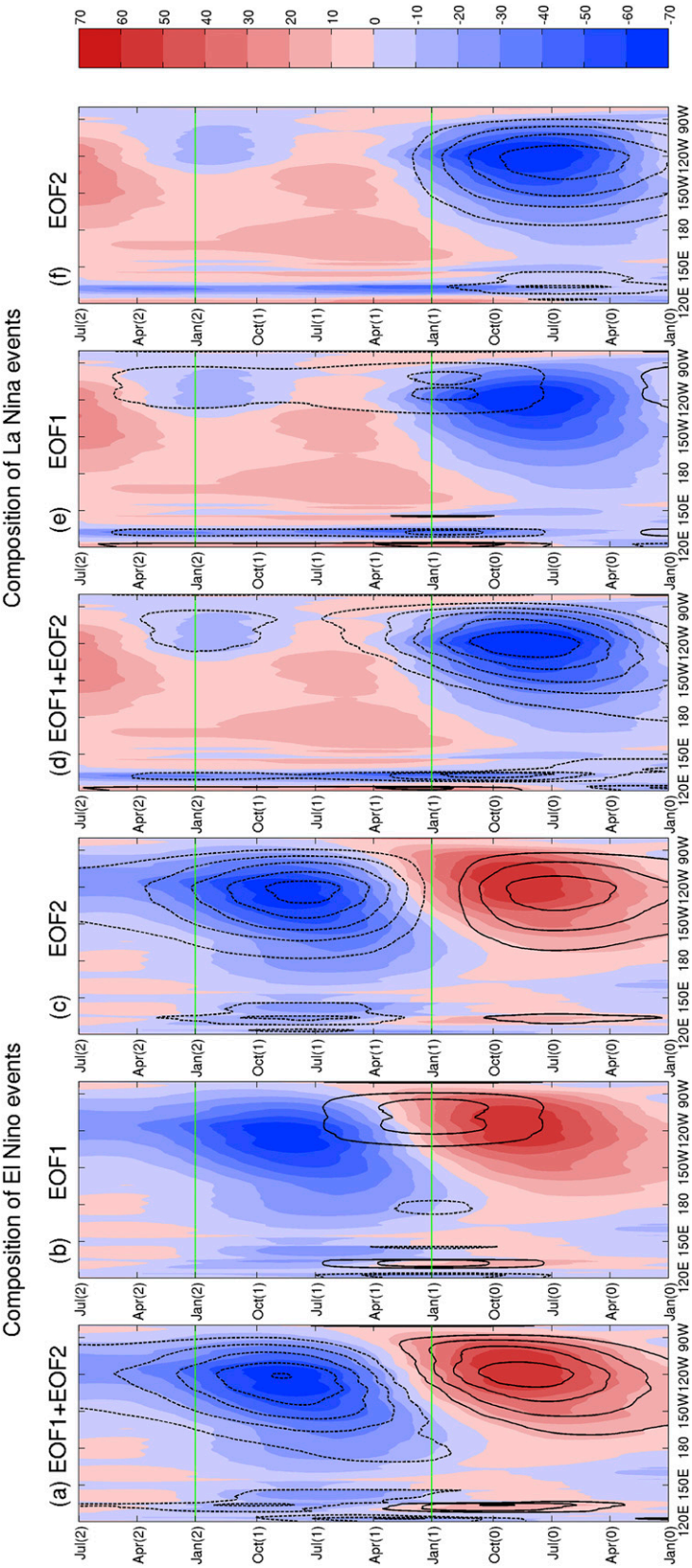

FIG. 6. Hovmöller diagram of reconstructed E anomalies for composite of (a)–(c) El Niño and (d)–(f) La Niña years. Color shadings are 15-month low-pass-filtered E anomalies without EOF analysis. Contours are the E anomalies, which are reconstructed by the (a),(d) first two EOFs together, (b),(e) just the EOF1, and (c),(f) just the EOF2 of 15-month low-pass D20 values. The interval of contours and shadings is 10 m. The green horizontal lines represent Jan(1) and Jan(2), respectively.

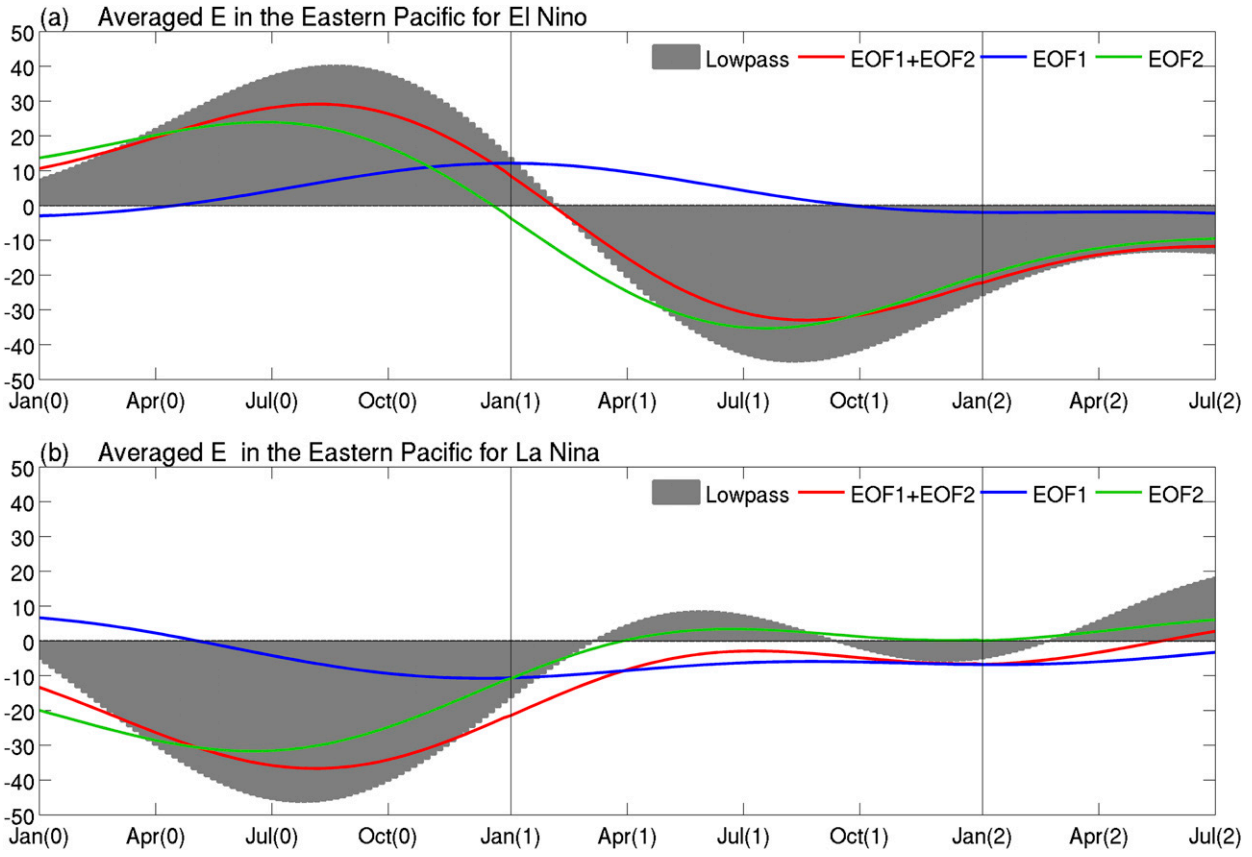

FIG. 7. As in Fig. 5, but for E anomalies. The gray area represents the E anomalies in original 15-month low-pass data. The red curves are the reconstructed E anomalies by EOF1 and EOF2. The blue (green) curves are the reconstructed E anomalies by EOF1 (EOF2).

same time as EOF1 (contours, Figs. 6b,e) reaches its peak. This result agrees with the lag between the tilting mode and recharge–discharge mode, which is a quarter of the period (Li 1997; Jin 1997a). It is noted that, although the EOF1 and EOF2 are stationary by themselves, the eastward propagating feature of the low-frequency process [i.e., the early reversal of zonal transport in Oct(0)–Nov(0)] appears as the combination of both the tilting mode (EOF1) and recharge–discharge mode (EOF2; Li 1997). Therefore, this propagation is not a result of high-frequency oceanic Kelvin waves but rather a result of the response of the two slow modes of the thermocline to surface wind forcing. In fact, the speed of propagation is much slower than the high-frequency ocean Kelvin waves.

In Fig. 7, the E anomalies averaged over the equatorial eastern Pacific region (5°S–5°N, 160°W–80°W) are shown to quantify the contribution. The E anomaly of the first two EOFs (red curve, Fig. 7) can reconstruct most amplitudes of low-frequency E anomalies (gray area, Fig. 7). The peaks and phase transition of the low-frequency process are dominated by the recharge–discharge mode. In contrast, the tilting mode only shifts the timing of the peaks and phase transition slightly. One should note that, during the development phase, the anomaly patterns of EOF1 and EOF2 are quite symmetric between El Niño and La Niña events (contour, Fig. 6). However, the asymmetric features appear after the peak. For El Niño, the positive E anomalies of EOF1 over the eastern Pacific switch to negative E anomalies after Oct(1), and the negative E anomalies of EOF2 are significant during Year(1). For La Niña, however, the negative E anomalies of EOF1 remain stationary in the eastern equatorial Pacific throughout Year(0) to Year(1) due to the stationary easterly surface wind anomalies (contour, Fig. 1), and the positive E anomalies associated with EOF2 are very weak during Year(2). This difference in the spatial pattern in the low-frequency process between El Niño and La Niña leads to the larger amplitude of the reversed zonal transport anomalies over the eastern Pacific in El Niño than that in La Niña (gray bar, Fig. 7). Then, the reversed zonal transport anomaly after the mature phase is more efficient in weakening an El Niño in the eastern Pacific than changing a La Niña because the zonal mean SST

advection by zonal current anomalies during El Niño is larger than that in La Niña.

c. *High-frequency process*

Although the interactions between the ocean and atmosphere at interannual time scales govern the evolution of the ENSO (Bjerknes 1969; Battisti 1988; Schopf and Suarez 1988; Kessler 2002), they are also strongly modulated by the high-frequency variability. The high-frequency oceanic Kelvin waves not only might influence the development of the ENSO by transporting warm or cold water eastward (Harrison and Schopf 1984; Fedorov and Melville 2000; Roundy and Kiladis 2006), but they also impact the evolution of the ENSO through zonal SST advection by changing the concavity of the anomalous meridional thermocline structure (Chen et al. 2016).

Figure 8 shows the propagation and reflection of high-pass-filtered D20 anomalies during El Niño and La Niña years. During the ENSO developing phases, there is an evident thermocline anomaly propagating from the western-central Pacific toward the eastern boundary in Jul(0)–Oct(0). This thermocline anomaly deepens (or shoals) toward the east over time, associated with the eastward propagation of the pronounced positive (or negative) ocean heat content anomalies along the equator during El Niño (or La Niña; Tseng et al. 2017a). The eastward propagating thermocline anomaly along the equator reaches the oceanic eastern boundary in boreal winter at the peak phase of ENSO. Subsequently, the D20 anomaly in the eastern boundary is reflected as Rossby waves and propagates westward off the equator in both hemispheres (Picaut et al. 1997; Chen et al. 2016). Afterward, the off-equatorial thermocline depth anomalies become more dominant in the eastern Pacific, and the meridional structure of the thermocline anomalies at the equator is reversed in the eastern Pacific (e.g., the off-equatorial thermocline depth anomalies become higher than those on the equator for El Niño events and lower for La Niña events). This change in thermocline structure would reverse the zonal geostrophic transport rapidly after the mature phase of ENSO (Figs. 4c,d).

The evolution of high-frequency oceanic waves can be represented using EOF analysis performed on the 15-month high-pass-filtered D20 in the equatorial region (10°S–10°N, 120°E–80°W). The first three spatial structures of EOFs are shown in Fig. 9, representing 13.0%, 7.1%, and 5.6% of the total variance of the high-pass-filtered D20. Although the first three EOFs can only explain a total of 25.7% of the variance of high-pass-filtered equatorial thermocline, they can adequately describe the wave dynamics in the tropical waveguide. The three EOFs indicate wave propagation along the equator (EOF1; Fig. 9a), wave arrival at the eastern boundary (EOF2; Fig. 9b), and wave reflection at the eastern boundary followed by westward propagation off the equator (EOF3; Fig. 9c). The first EOF leads the second EOF by one month (correlation coefficient is 0.48), and the second EOF leads the third EOF by 1.3 months (correlation coefficient is 0.32). The composites of the D20 anomalies related to the three EOFs for the El Niño and La Niña events are also shown in Fig. 10. The timing is chosen by the maximum spatial correlation between the composite of D20 anomalies and the EOF pattern during the ENSO mature phase to the early decaying phase, and the corresponding timing is shown as dashed black lines in Fig. 8. The intervals between these three stages are 0.8 and 1.5 months for El Niño events, and 0.8 and 1.8 months for La Niña events, consistent with the time scale in the EOF analysis. The spatial pattern of the D20 anomaly composite in Fig. 10 is highly correlated with the first three EOFs. The corresponding timing of these three patterns (Fig. 8) also indicates the three stages of the ocean wave process: wave propagation along the equator, wave arrival at the eastern boundary, and the reflection and westward propagation off the equator. The rest of the modes are not significant to the wave dynamics associated with the ENSO cycle. The variances of the fourth and fifth modes only represent 3.5% and 2.9%, respectively, of the total variance in D20. Furthermore, the spatial correlation coefficients between the D20 composite and the fourth EOF pattern from the ENSO mature phase to the early decaying phase are less than 0.35 for El Niño events and less than 0.25 for La Niña events. The results demonstrate that equatorial wave dynamics associated with ENSO evolution can be captured by just the first three EOFs.

The shading in Fig. 11 shows high-pass-filtered E anomalies with the reconstructed signal from EOF1 + EOF2 + EOF3 superimposed as contours. The reconstructed E anomalies (contours) provide a good overall fit to the E anomalies with high-pass filter (shading), indicating that the three stages of wave dynamics based on EOFs can well represent the high-frequency process. The time series of reconstructed E anomalies averaged over the eastern Pacific (red curves) exhibits almost the same amplitude and variability with the high-pass-filtered E anomalies (Fig. 12). Those results demonstrate that the equatorial zonal transport associated with the concavity of meridional thermocline anomalies can be represented by equatorial wave dynamics captured by the first three EOFs.

The high-frequency equatorial oceanic Kelvin waves can be excited by westerly wind bursts or easterly wind

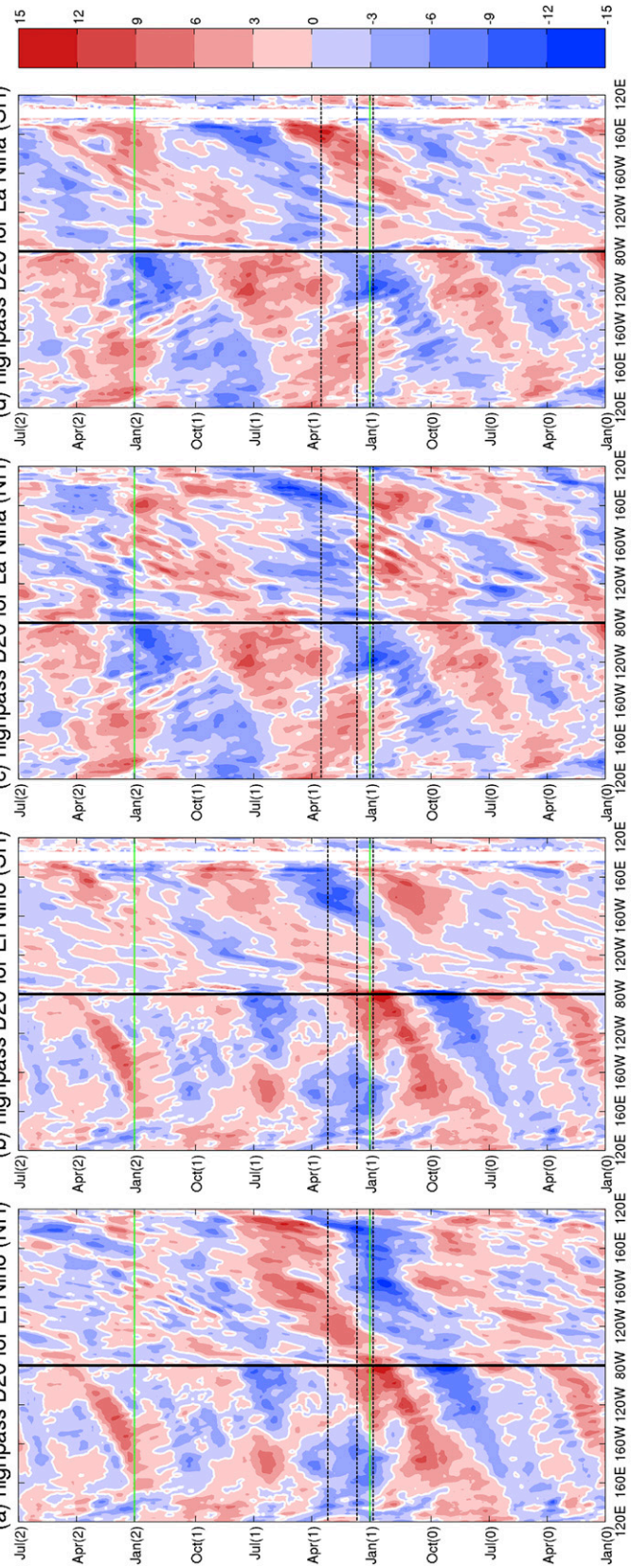

FIG. 8. Hovmöller diagram of D20 anomalies along (5°S–5°N) and off the equator for composite of (a),(b) El Niño and (c),(d) La Niña years, for (a),(c) the Northern Hemisphere (5°N–10°N) and (b),(d) the Southern Hemisphere (5°–10°S). The interval is 3 m. The boundary between the two regions is shown by vertical black lines. The green lines represent Jan(1) and Jan(2), respectively. (The dashed black lines indicate the corresponding timing with EOF1, EOF2, and EOF3 in Fig. 9.)

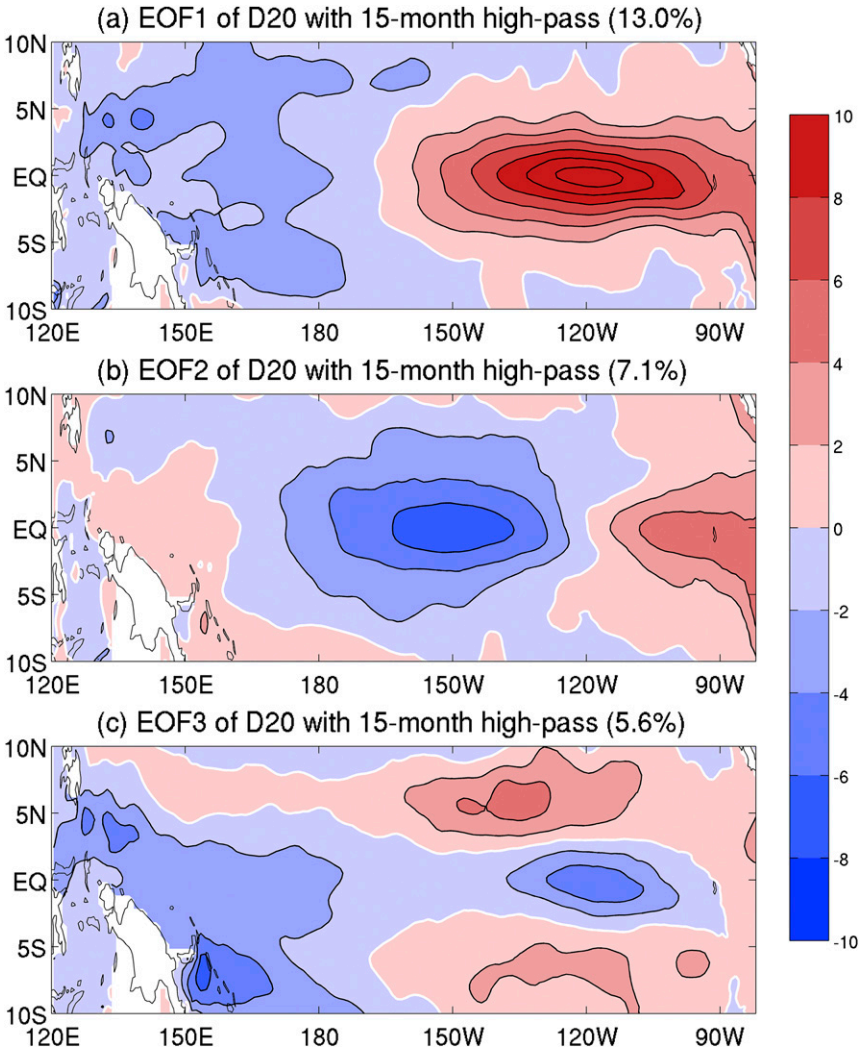

FIG. 9. First three spatial structures of the EOF analysis—EOFs (a) 1, (b) 2, and (c) 3— fit to a 15-month high-pass D20 in the region 10°S–10°N, 120°E–80°W. The interval is 2 m for D20 anomalies and the white curves represent zero D20.

surges (e.g., McPhaden and Yu 1999; Delcroix et al. 2000; Kessler 2002; Roundy and Kiladis 2006; Fedorov et al. 2015; Tseng et al. 2017a). The WWBs and EWSs, synoptic-scale disturbances that occur near the equator, are considered to have a large impact on ENSO evolution. To investigate the relationship between the oceanic Kelvin waves and surface wind forcing in high-frequency processes, the Hovmöller diagram of D20 anomalies (shading) is shown in Fig. 13. These anomalies are depicted along the equator, superimposed by the near-surface zonal wind anomalies (contour) averaged between 5°S–5°N, to obtain the composites for El Niño and La Niña. The existence of a sequence of eastward propagation of downwelling (upwelling) Kelvin waves associated with WWBs (EWSs) is evident in the western-central Pacific. The eastward propagation is more evident in the El Niño events than in the La Niña events due to the deepening signal that can be easily detected when the thermocline is shallower in the central-eastern tropical Pacific for El Niño events. It is noted that the abrupt increase and eastward migration of WWBs–EWSs were found over the Pacific during the ENSO developing phase [Year(0)]. The major WWBs–EWSs occur in boreal summer and fall with coincident downwelling (upwelling) Kelvin waves for El Niño (La Niña) events. Then, the signal of Kelvin waves reaches the eastern boundary in boreal winter and reflect as off-equator Rossby waves. A key question is why and how the WWEs–EWSs occur during the ENSO developing phase [Jul(0)–Oct(0)].

Several studies have suggested that WWB occurrences are not random but are greatly influenced by

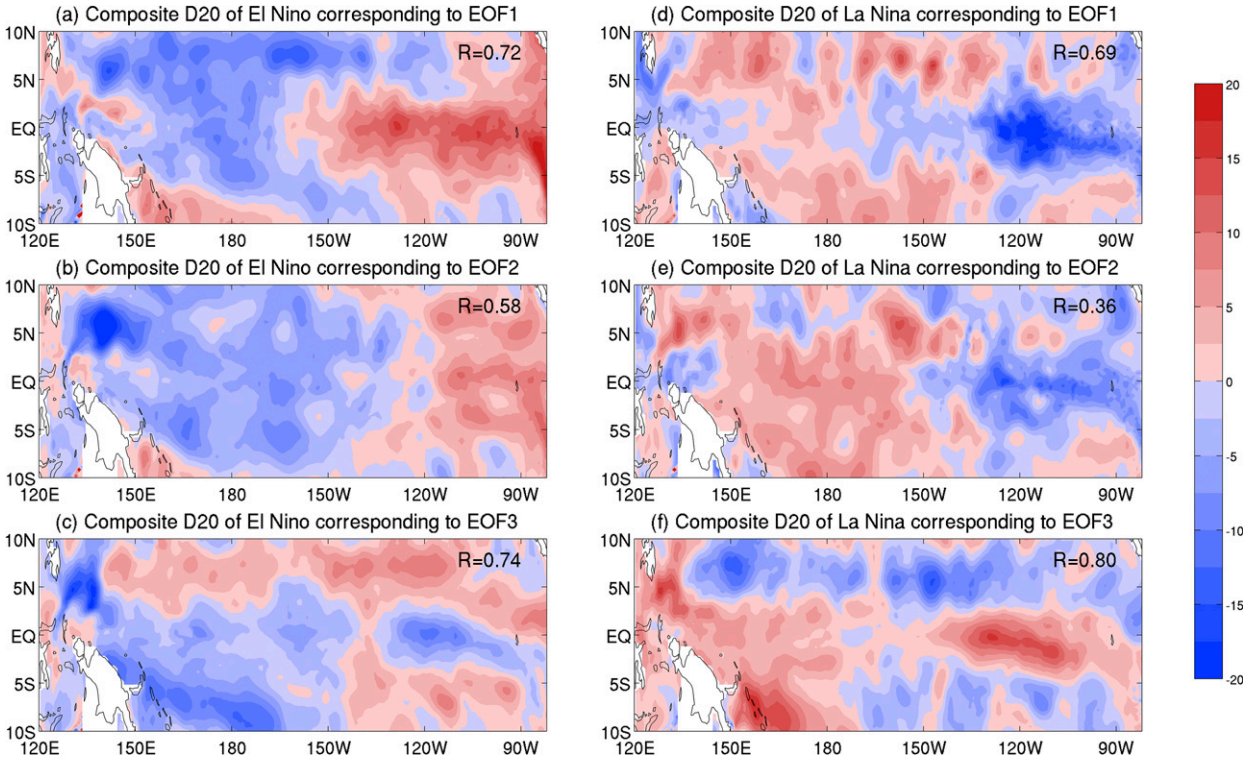

FIG. 10. Composites of the D20 anomalies for (a)–(c) El Niño and (d)–(f) La Niña years. The timing is chosen so the spatial correlation between composites of the D20 and EOF pattern is at a maximum during the ENSO mature phase to early decaying phase. The spatial correlation coefficients are displayed on the top-right corner of the panel. The corresponding timing is shown as dashed black lines in Fig. 8. The interval for the D20 anomalies is 5 m. The color scale on the right runs from 20 m at the top to −20 m at the bottom in increments of 5 m.

interaction with large-scale environment variations associated with ENSO evolution (Lengaigne et al. 2003, 2004; Eisenman et al. 2005; Roundy and Kiladis 2006; Seiki and Takayabu 2007). Seiki and Takayabu (2007) indicated that a strong MJO amplitude is only a favorable condition but not a sufficient condition for WWBs generation. Some modeling studies have also suggested that feedback between SST and WWBs can significantly affect the characteristics and dynamical regime of the ENSO system (Eisenman et al. 2005; Perez et al. 2005; Gebbie et al. 2007) instead of MJO. The WWB occurrences are modulated by the low-frequency SST variation (Eisenman et al. 2005; Tziperman and Yu 2007; Gebbie and Tziperman 2009) and are likely to occur when the warm pool is extended eastward during the ENSO developing phase (Yu et al. 2003; Eisenman et al. 2005), regardless of any MJO event. Miyama and Hasegawa (2014) found that the WWBs in 2002/03 El Niño event could be enhanced by the SST gradient in the western Pacific warm pool. In fact, we also show that the WWBs–EWSs abruptly increase and move eastward during the ENSO developing phase [last half of Year(0)]. The enhanced WWEs–EWSs further increase the downwelling (upwelling) oceanic equatorial Kelvin wave response.

4. Discussion

The change in the accumulated warm water volume via the recharge–discharge process in the tropics serves as a precondition and plays a dominant role in the low-frequency ENSO cycle (Jin 1997a). However, not all large WWV events in the tropical central Pacific would lead to an expected ENSO event. The eastward propagation of Kelvin waves arising from the ocean–atmosphere coupling is another necessary contribution to trigger ENSO development (Tseng et al. 2017a). Following the high-frequency process results shown in section 3c, Figs. 14 and 15 show the evolution of D20 (shading) and surface zonal wind anomalies (contour) for six El Niño (strong: 1982 and 1997; moderate: 1986, 1991, 2002, and 2009) and five La Niña (strong: 1988; moderate: 1998, 1999, 2007, and 2010) events. Although each ENSO event is unique, the WWBs–EWSs during the ENSO developing phase in all events play a significant role in the growth of the ENSO in the eastern

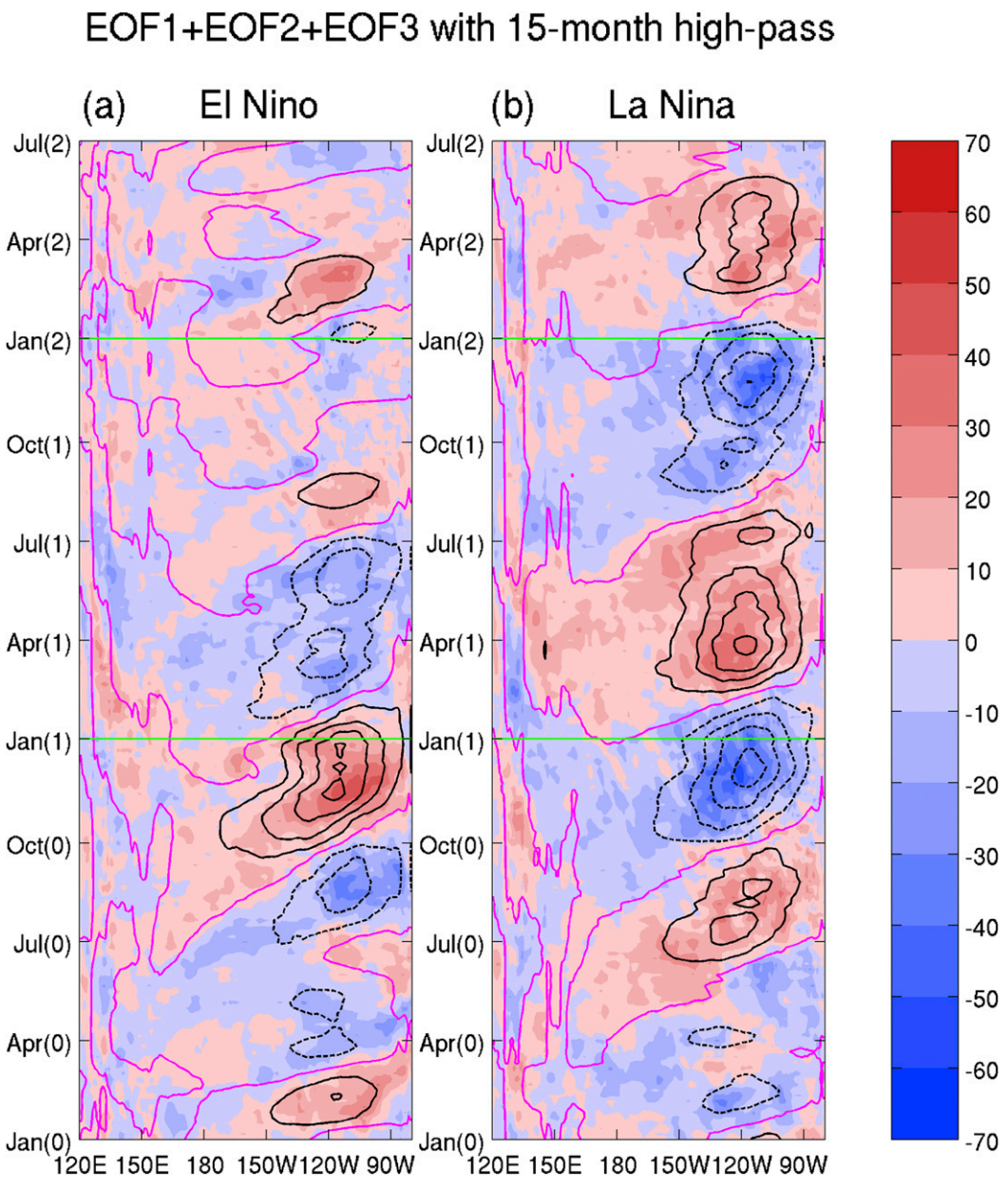

FIG. 11. Hovmöller diagram of reconstructed *E* anomalies (m) averaged between 5°S and 5°N for the composite of (a) El Niño and (b) La Niña years. Color shadings represent a 15-month high-pass filtering. Contours are *E* anomalies reconstructed by the first three EOFs of the 15-month high-passed D20. The purple lines represent the zero value of the contours. The interval of shadings and contours is 10 m. The green lines represent Jan(1) and Jan(2), respectively.

Pacific. For instance, the appearance of an anomalous warming in the central-eastern Pacific coincided with the eastward propagation of the downwelling Kelvin waves generated by the WWBs over western Pacific (McPhaden and Yu 1999). The warming in the eastern Pacific increased the gradient of zonal SST anomalies and enhanced the westerly wind anomalies over the central Pacific that further enhanced the eastern warming, leading to the development of El Niño (i.e., Bjerknes feedback). The WWBs likely occur in the location of the warm pool extending edge (Yu et al. 2003). When the Bjerknes instability is beyond a certain threshold, the local ocean–atmosphere feedback becomes extensive and triggers the global impact from the change in the Walker circulation. Then, WWBs strengthen and migrate eastward with a sequence of

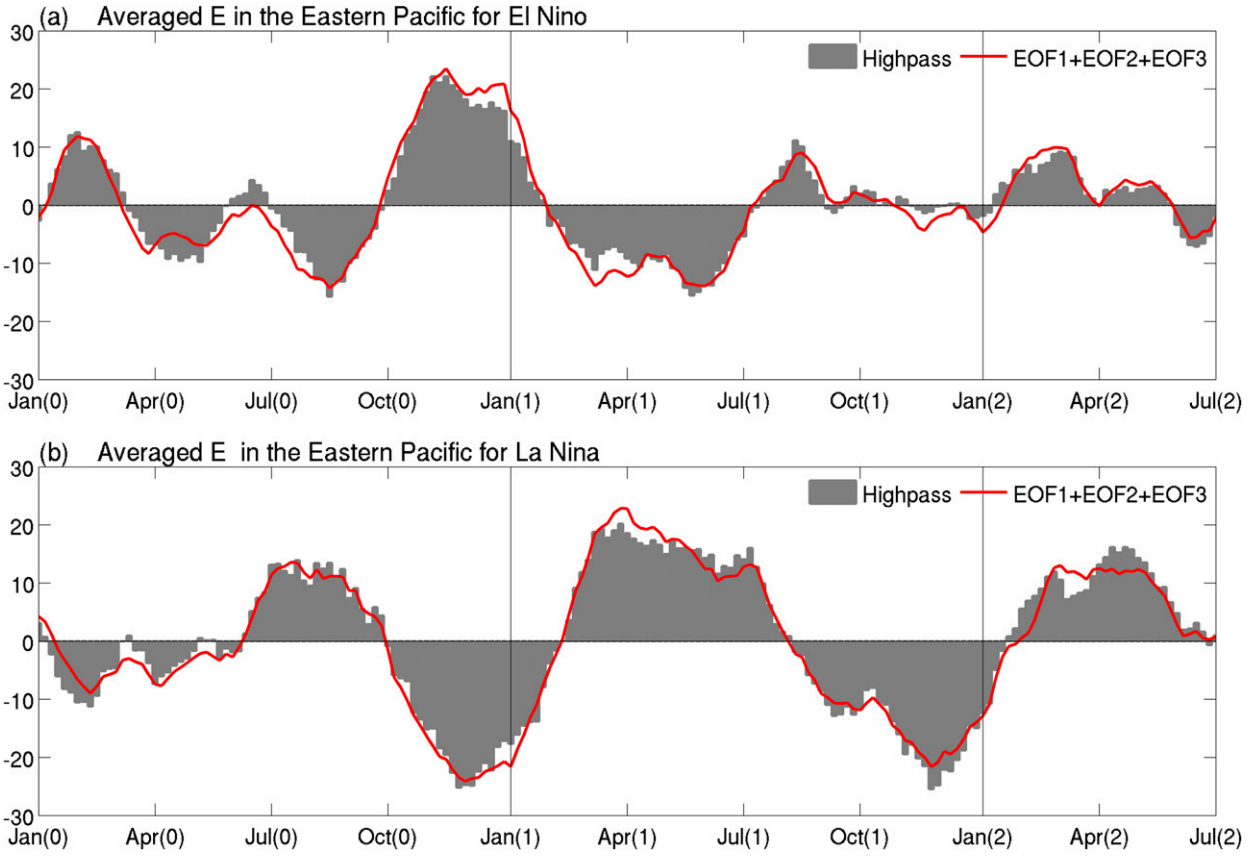

FIG. 12. The E anomalies averaged over the equatorial eastern Pacific region (5°S–5°N, 160°–80°W) for (a) El Niño and (b) La Niña years. The gray areas are the E anomalies in the original 15-month high-pass data. The red curves are the reconstructed E anomalies using the first three EOFs.

wave propagation in the ocean, and a medium to large ENSO event occurs due to the accumulation of the wave propagation process. In all El Niño (La Niña) events, the last downwelling (upwelling) Kelvin wave before the peak (black dashed lines, Figs. 14 and 15) is caused by the evident anomalous westerlies (easterlies) that commonly precede the peak by two to three months. The spatial pattern of D20 anomalies related to the three EOFs for the strongest El Niño (1997) and La Niña (1988) events are shown in Fig. 16. The D20 patterns in the 1997 and 1988 events are similar to the EOFs in Fig. 9 and the composite pattern in Fig. 10. Figure 16 clearly supports the three stages of the ocean wave process: the wave propagates along the equator (Figs. 16a,d), the wave reaches the eastern boundary (Figs. 16b,e), and the wave reflects and propagates westward off the equator (Figs. 16c,f). This oceanic propagation is more evident in the El Niño years than in the La Niña years because the deepening signal is easier to detect, but the shoaling thermocline is commonly entangled with the already shallow thermocline in the eastern Pacific. The downwelling (upwelling) Kelvin waves would fuel the events to reach their peak (green lines, Figs. 14 and 15). In summary, the development of ENSO is determined mainly by the low-frequency mode associated with the coupled ocean–atmosphere feedback (high-frequency mode), while the high-frequency mode associated with oceanic wave propagation plays a triggering role.

We also note that the propagation in all El Niño events has a similar phase speed of approximately 40° month^{-1} ($\sim$1.7 m s^{-1}), which is much slower than the free oceanic Kelvin wave speed of 2.7 m s^{-1} (Fedorov 2010). The slower propagation speed may be due to the air–sea coupling (Lau 1981; Roundy and Kiladis 2006). It is noted that the propagation speed in La Niña events is approximately 30° month^{-1} ($\sim$1.3 m s^{-1}), which is slower than in El Niño events. According to most theoretical treatments of oceanic Kelvin waves, a deeper thermocline should result in faster eastward propagation (Long and Chang 1990). That is to say, the propagation speed is faster in El Niño events because of the deeper thermocline.

As we mention in the previous sections, there is a significant asymmetry in the spatial and temporal pattern

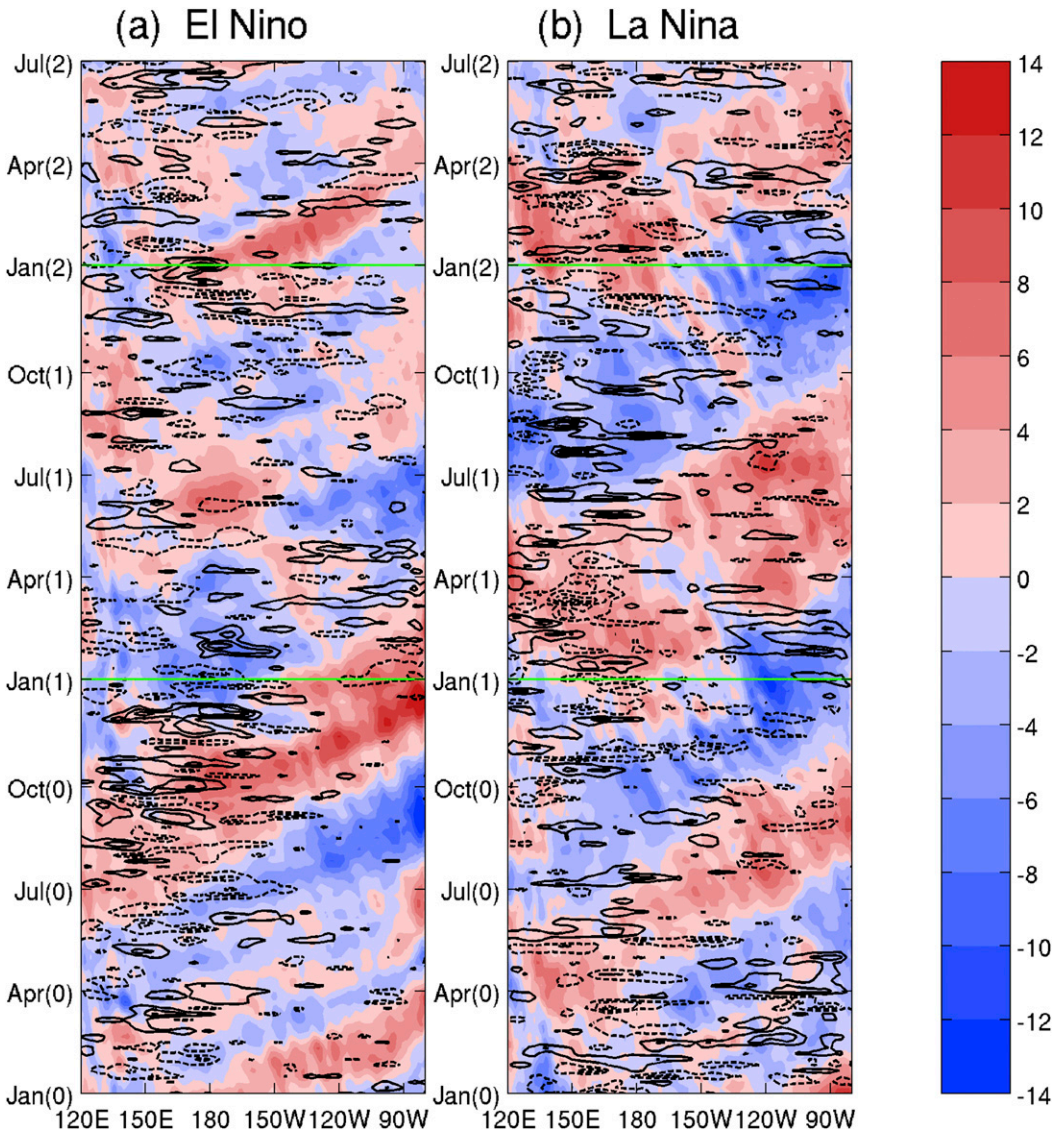

FIG. 13. As in Fig. 11, but for the 15-month high-pass-filtered D20 anomalies (color shading) and the near-surface zonal wind (contours). The interval is 2 m for the D20 anomalies and 0.5 m s^{-1} for the zonal wind anomalies (solid curves are positive and dashed curves are negative).

between El Niño and La Niña. The results from Fig. 5 indicate that the amplitude of the unfiltered zonal transport anomaly after the peak (gray bar, Fig. 5) is larger in El Niño (the peak is about −1.01 Sv; 1 Sv ≡ 10^6 m^3 s^{-1}) than in La Niña (the peak is about 0.53 Sv). That is to say, the weakening of ENSO events due to the zonal transport anomaly reversal after the mature phase in El Niño is more efficient than that in La Niña. This asymmetry of the ENSO after the mature phase results from a different amplitude for low-frequency zonal transport between El Niño and La Niña. For El Niño, the amplitude of the low-frequency zonal transport anomaly during the decaying phase [Year(1)] can reach −0.78 Sv; however, the low-frequency reversed transport anomaly is only 0.22 Sv for La Niña. Compared to low-frequency zonal transport, the amplitude of the high-frequency zonal transport anomaly after the mature phase is similar between El Niño and La Niña events (the maximum amplitude is about 0.29 Sv). This result indicates that the total zonal transport anomaly (gray area, Fig. 5) during the decaying phase is dominated more by low-frequency processes in El Niño events because the amplitude of the low-frequency transport anomaly (red curves, Fig. 5a) is larger than that of the high-frequency anomaly (blue curves, Fig. 5a). However, the transport anomaly is caused by both low-frequency

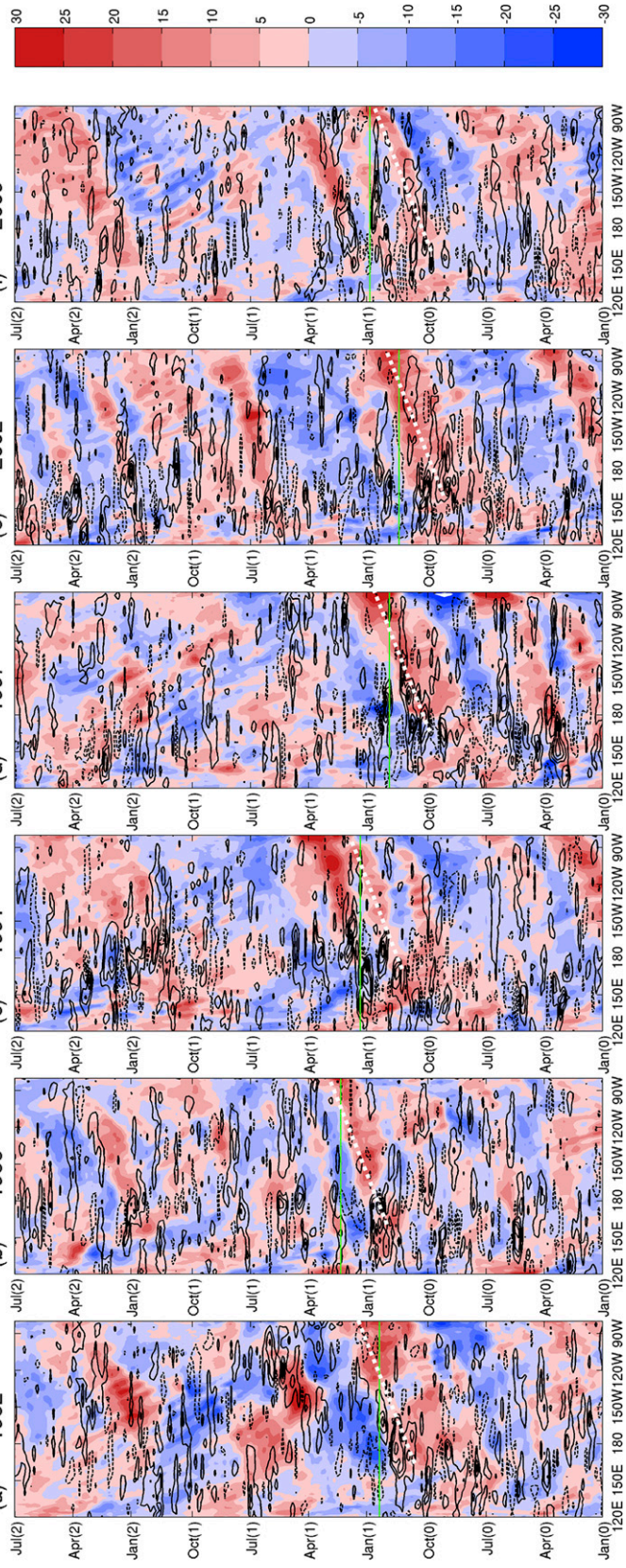

FIG. 14. Hovmöller diagram of the 15-month high-pass-filtered D20 anomalies (color shading) and near-surface zonal wind anomalies (contours) averaged between 5°S and 5°N for seven El Niño events (a)–(f) between 1882 and 2009. White dashed lines are approximate trajectories of the major propagation for 40° month^{-1}. The green lines represent the peak of El Niño event. The interval is 5 m for D20 anomalies, and 1.5 m s^{-1} for zonal wind anomalies (solid curves are positive and dashed curves are negative). The color scale on the right runs from 30 m at the top to −30 m at the bottom in increments of 5 m.

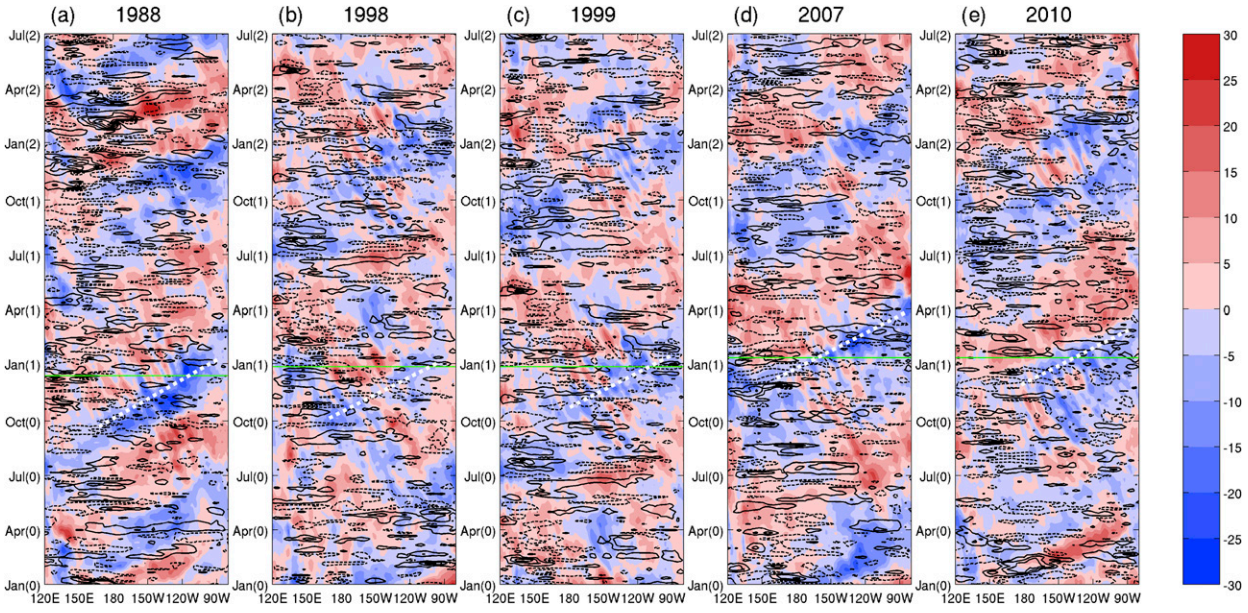

FIG. 15. As in Fig. 14, but for five La Niña events (a)–(e) between 1988 and 2010; the white dashed lines are approximate trajectories of the major propagation at a speed of 30° month^{-1}.

and high-frequency processes during La Niña because of the equivalent amplitudes between the low-frequency and high-frequency transport anomalies (red and blue curves, respectively in Fig. 5b).

In the last two decades, two types of ENSO events have been categorized (Larkin and Harrison 2005; Ashok et al. 2007; McPhaden et al. 2011). One is called the eastern Pacific (EP) ENSO, which has its major SST

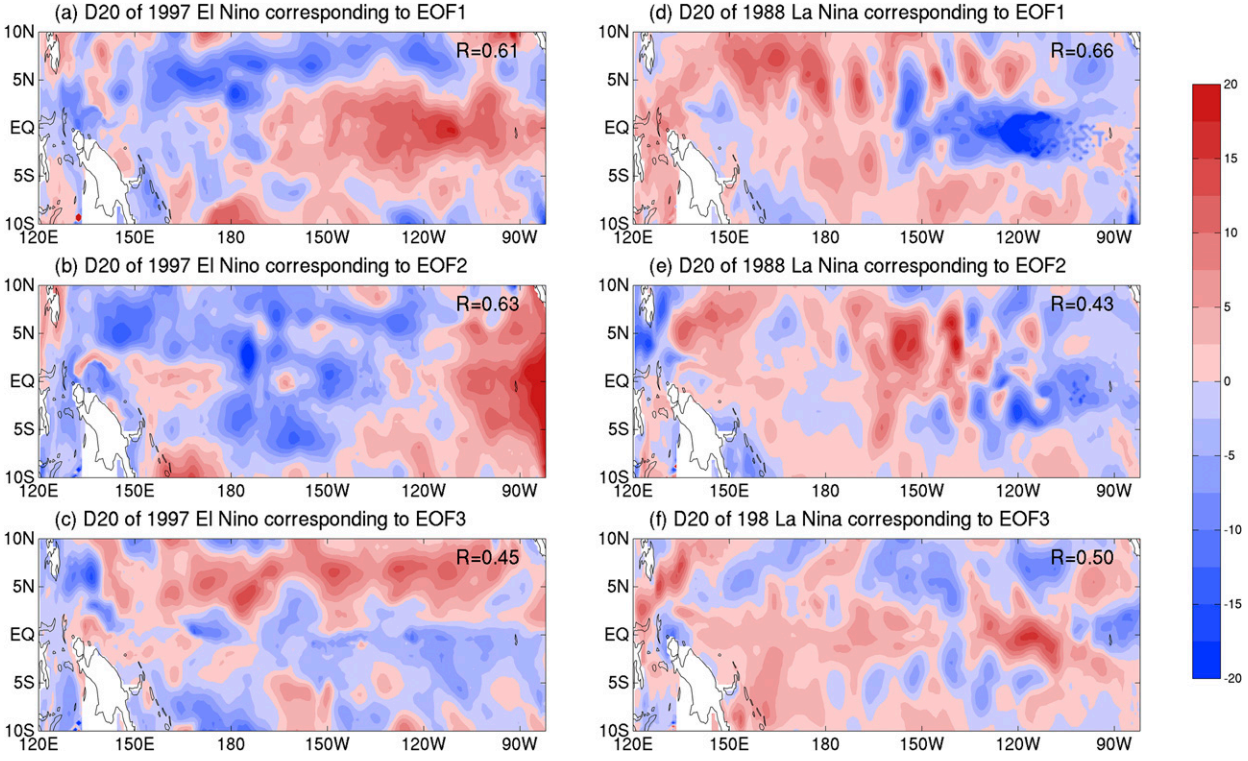

FIG. 16. As in Fig. 10, but for the (a)–(c) 1997 El Niño event and (d)–(f) 1988 La Niña event.

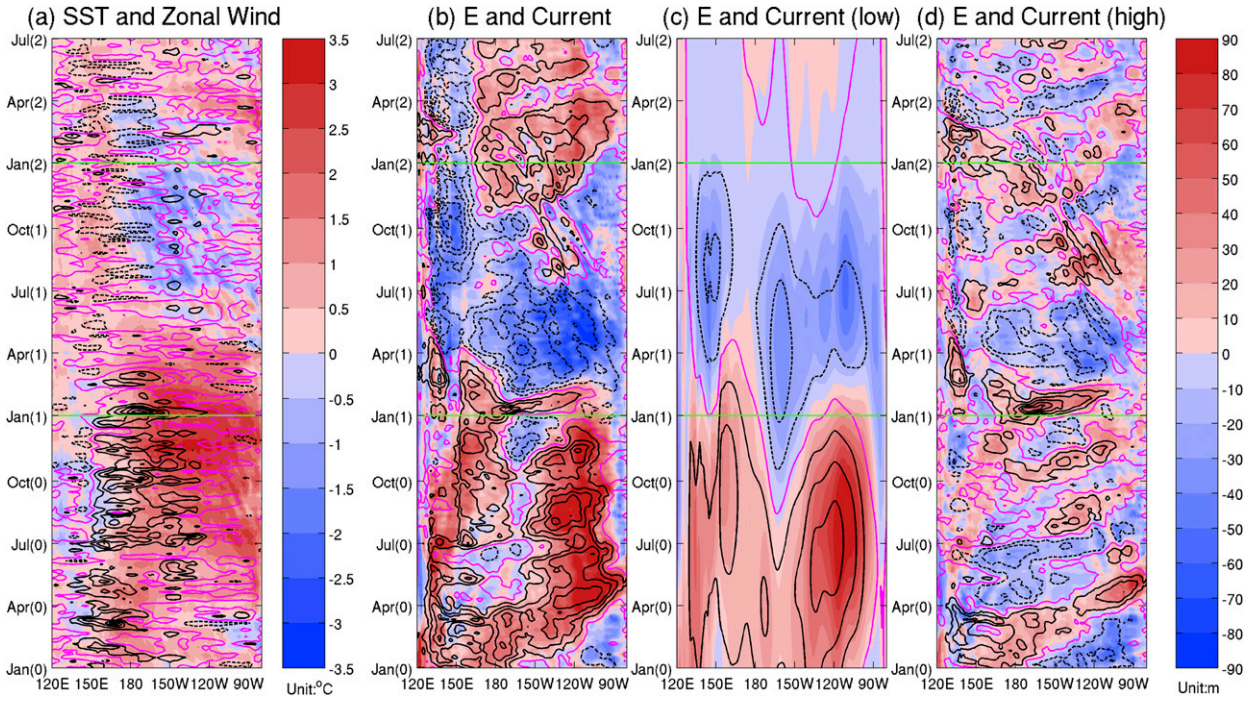

FIG. 17. Hovmöller diagram of (a) SST anomalies (color shading) and near-surface wind anomalies (contours) and (b)–(d) *E* anomalies (contours) and zonal transport anomalies (color shading) for the 2015/16 El Niño event. The data in (c) and (d) have been filtered by a 15-month low and high pass filter, respectively. The green lines represent Jan(1) and Jan(2), respectively. In (a), the interval is in 0.5°C for SST and 2 m s^{-1} for zonal wind anomalies. In (b)–(d), the contour interval is 1 Sv for transport anomalies and shading interval is 10 m for *E* anomalies. The solid (dashed) contours represent positive (negative) values, and the purple contours represent zero values.

anomalies centered in the equatorial eastern Pacific (Kao and Yu 2009). The other is the central Pacific (CP) ENSO, which is characterized by the largest SST anomalies in the equatorial central Pacific. Although both types of ENSO differ in patterns, triggers, amplitudes, and time evolution, the oceanic processes proposed in this study are similar. For the low-frequency component, the recharge–discharge process is similar regardless of ENSO type, except for the zonally different center locations of the SST anomalies, surface wind anomalies, and thermocline variation patterns (Ren and Jin 2013). The westward-shifted patterns are crucial for the westward shift in the zonal transport anomalies in the CP ENSO. The role of the high-frequency component is also the same in these two ENSO types. Figure 14 shows that there is no significant difference between the EP El Niño (1982/83, 1986/87, and 1997/98) and the CP El Niño (1991/92, 2002/03, and 2009/10) cases. In all El Niño events, the last downwelling Kelvin wave caused by the evident anomalous westerlies propagates eastward before the peak.

The strong El Niño event in 2015/16 is unique compared to many previous El Niño events and is a specific example. Figure 17 shows the Hovmöller diagram of SST, near-surface wind, zonal transport, and *E* index in 2015/16, supporting an evolution of SST anomalies and near-surface winds (Fig. 17a) similar to previous El Niño events (Fig. 1a). Consistent with the discussion above, a series of WWBs during the first quarter of 2015 (contour, Fig. 17a) resulted in the eastward propagation of downwelling oceanic Kelvin waves (not shown). These Kelvin waves generated eastward transport in the central and eastern Pacific during the developing phase associated with the strengthened positive SST anomalies (shading, Fig. 17a) in the eastern Pacific. Similar to the typical evolution of El Niño, the first reversed zonal transport anomaly driven by the local wind forcing appears during Oct(0)–Nov(0) between 150°E and the date line (Fig. 17b). One of the distinct aspects of the 2015/16 El Niño event, compared to previous events, is an eastward transport, occurring during Jan(1)–Feb(1) around the date line. This eastward transport is attributed to the high-frequency transport (Fig. 17d), which was generated by strong WWBs during Jan(1)–Feb(1) (Fig. 17a), resulting from the persistent development of El Niño and amplified by the tropical–extratropical teleconnection in the North Pacific (Di Lorenzo and Mantua 2016; Tseng et al. 2017b). After this, a basinwide reversal of the zonal transport anomalies resulting from the low-frequency recharge–discharge process (Fig. 17c)

and high-frequency oceanic wave process (Fig. 17d) occurs and weakens the existing SST anomalies. Our result indicates that the basinwide current reversal mechanism is a robust ocean dynamic process and also works perfectly in 2015/16 El Niño.

In this study, only moderate and strong ENSO events are used in the composite analysis. In general, the oceanic process holds for medium to large ENSO events definitely due to large ocean energy sources. It also works well for weak ENSO events because the recharge–discharge and wave propagating processes occur commonly in the central tropical Pacific. However, the signal may not be as strong and the time scale would be different (normally shorter in the weak ENSO events). To focus on the oceanic processes, only moderate and strong ENSO events were selected. Note that the evolution of SST anomalies indicates a distinct pattern of El Niño decaying processes (Lee et al. 2014). Although many other factors can contribute to the decaying of ENSO events, most events reach their peak intensity near boreal winter. That is, the basinwide current reversal mechanism is a robust ocean dynamic process built in to the peak phase of ENSO as a dynamic feedback within the ocean for both El Niño and La Niña.

5. Summary

The oceanic processes of sudden reversal of the zonal equatorial transport anomaly above the thermocline at the peaking phase of ENSO are decomposed into a low-frequency ENSO cycle and a high-frequency oceanic wave process. Both processes can be represented by the concavity of the meridional thermocline anomaly, and they can reverse the zonal equatorial transport anomaly at the peaking phase of ENSO, which is a trigger for the rapid termination of an ENSO event.

For the low-frequency process, known as the recharge–discharge mode, the equatorial zonal transport presents a gradual and basinwide evolution. During the El Niño (La Niña) developmental phase, the eastward (westward) transport anomaly prevails in the central-eastern Pacific and enhances ENSO growth through zonal temperature advection. In Oct(0)–Nov(0), the gradual reversal of the zonal transport anomaly is initiated near the date line due to the Sverdrup transport, which is associated with local wind forcing. After that, a basinwide reversal of transport and E anomalies occurs around Jan(1). This basinwide transport reversal weakens the ENSO SST anomalies through advection damping. Furthermore, an EOF analysis was performed on the 15-month low-pass-filtered D20 in the equatorial region to discuss the first two oceanic leading modes, the east–west tilting mode and the recharge–discharge mode. The propagated feature of the low-frequency process, the early reversal of zonal transport in Oct(0)–Nov(0), is caused by the tilting process in which the concavity of meridional thermocline is determined by the equatorial thermocline depth anomalies. By contrast, the amplitude and phase transition of zonal transport are mainly determined by the recharge–discharge process.

Compared to the low-frequency process, the high-frequency zonal transport exhibits significant eastward propagation, and the reversals of the high-frequency transport are more rapid than those of the low-frequency transport. During the developing year, a series of eastward-moving disturbances consistent with eastward transport and westward transport are related to the Kelvin wave at the equator. The major WWEs–EWSs occur in boreal summer and fall from Jul(0) to Oct(0) with coincident downwelling (upwelling) Kelvin waves for El Niño (La Niña) events. After the peak of El Niño (La Niña), the signal of the Kelvin waves reaches the eastern boundary in boreal winter, and is reflected as off-equator Rossby waves. Then, the zonal transport switches from eastward (westward) to westward (eastward). As a result, the off-equatorial thermocline depth anomalies become more dominant in the eastern Pacific. The results of EOF analysis indicate that the first three EOFs can adequately describe the wave dynamics in the tropical waveguide. To be more precise, although the first three EOFs can explain only 25.7% of the variance of the high-pass-filtered equatorial thermocline, the equatorial zonal transport associated with the concavity of meridional thermocline anomalies can definitely be represented by the equatorial wave dynamics captured by the first three EOFs.

We demonstrate that the role of wave dynamics is as important as the recharge–discharge mode during the phase transition of the ENSO. Both the recharge–discharge mode and wave dynamics can be represented by the meridional structure of thermocline anomalies, as both processes are in phase after the current reversal. Jin and An (1999) indicate that the zonal advective feedback is dynamically linked with the thermocline feedback of the recharge–discharge process via geostrophic balance. In recharge–discharge theory, the equatorial Sverdrup balance, mass conservation, and off-equatorial Sverdrup balance determine the slow response to slowly varying winds. However, they assume that wave propagation is a relatively fast process, which quickly establishes the Sverdrup balances on and off the equator. Here, we emphasize that the oceanic wave processes cannot be ignored, especially in La Niña events. Both high-frequency ''wave dynamics'' and the low-frequency ''recharge–discharge mode'' play distinct

roles in the ENSO variability with specific emphasis on different time scales. For the high-frequency process, most of the previous studies focus on the role that westerly wind bursts (WWBs) may play in the development of El Niño (Wyrtki 1975; McPhaden and Yu 1999; Lengaigne et al. 2004; Gebbie et al. 2007). In our study, however, we focus on how the WWBs could facilitate the transition of an ENSO event via high-frequency oceanic wave dynamics. As a result, the combined role of low-frequency and high-frequency oceanic processes could adequately explain the sudden termination of an ENSO event and provide an additional remark of phase locking. The physical connection between low-frequency and high-frequency oceanic processes and the robustness of the results need to be further examined using model simulations.

Acknowledgments. This work is supported by the Ministry of Science and Technology (MOST 105-2119-M-002-025 and 106-2111-M-002-003-MY2). Y.-H. Tseng is supported by the MOST Grant 106-2111-M-002-001. B. Huang is supported by grants from NOAA (NA14OAR4310160 and NA17OAR4310144) and NASA (NNX14AM19G). The authors thank all colleagues and students who contributed to this study.

REFERENCES

An, S.-I., and F.-F. Jin, 2001: Collective role of thermocline and zonal advective feedbacks in the ENSO mode. *J. Climate*, **14**, 3421–3432, https://doi.org/10.1175/1520-0442(2001)014<3421:CROTAZ>2.0.CO;2.

Ashok, K., S. K. Behera, S. A. Rao, H. Weng, and T. Yamagata, 2007: El Niño Modoki and its possible teleconnection. *J. Geophys. Res.*, **112**, C11007, https://doi.org/10.1029/2006JC003798.

Battisti, D. S., 1988: Dynamics and thermodynamics of a warming event in a coupled tropical atmosphere–ocean model. *J. Atmos. Sci.*, **45**, 2889–2919, https://doi.org/10.1175/1520-0469(1988)045<2889:DATOAW>2.0.CO;2.

——, and A. C. Hirst, 1989: Interannual variability in a tropical atmosphere–ocean model: Influence of the basic state, ocean geometry and nonlinearity. *J. Atmos. Sci.*, **46**, 1687–1712, https://doi.org/10.1175/1520-0469(1989)046<1687:IVIATA>2.0.CO;2.

Behringer, D. W., and Y. Xue, 2004: Evaluation of the Global Ocean Data Assimilation System at NCEP: The Pacific Ocean. *Eighth Symp. on Integrated Observing and Assimilation Systems for Atmosphere, Oceans, and Land Surface*, Seattle, WA, Amer. Meteor. Soc., 2.3, https://ams.confex.com/ams/pdfpapers/70720.pdf.

Bjerknes, J., 1969: Atmospheric teleconnections from the equatorial Pacific. *Mon. Wea. Rev.*, **97**, 163–172, https://doi.org/10.1175/1520-0493(1969)097<0163:ATFTEP>2.3.CO;2.

Chen, H.-C., Z.-Z. Hu, B. Huang, and C.-H. Sui, 2016: The role of reversed equatorial zonal transport in terminating an ENSO event. *J. Climate*, **29**, 5859–5877, https://doi.org/10.1175/JCLI-D-16-0047.1.

Chiodi, A. M., and D. E. Harrison, 2015: Equatorial Pacific easterly wind surges and the onset of La Niña events. *J. Climate*, **28**, 776–792, https://doi.org/10.1175/JCLI-D-14-00227.1.

Delcroix, T., B. Dewitte, Y. duPenhoat, F. Masia, and J. Picaut, 2000: Equatorial waves and warm pool displacements during the 1992–1998 El Niño Southern Oscillation events: Observation and modeling. *J. Geophys. Res.*, **105**, 26 045–26 062, https://doi.org/10.1029/2000JC900113.

Di Lorenzo, E., and N. Mantua, 2016: Multi-year persistence of the 2014/15 North Pacific marine heatwave. *Nat. Climate Change*, **6**, 1042–1047, https://doi.org/10.1038/nclimate3082.

Eisenman, I., L. Yu, and E. Tziperman, 2005: Westerly wind bursts: ENSO's tail rather than the dog? *J. Climate*, **18**, 5224–5238, https://doi.org/10.1175/JCLI3588.1.

Emery, W. J., and R. E. Thomson, 2001: *Data Analysis Methods in Physical Oceanography.* Elsevier Science, 654 pp.

Fedorov, A. V., 2010: Ocean response to wind variations, warm water volume, and simple models of ENSO in the low-frequency approximation. *J. Climate*, **23**, 3855–3873, https://doi.org/10.1175/2010JCLI3044.1.

——, and W. K. Melville, 2000: Kelvin fronts on the equatorial thermocline. *J. Phys. Oceanogr.*, **30**, 1692–1705, https://doi.org/10.1175/1520-0485(2000)030<1692:KFOTET>2.0.CO;2.

——, S. Hu, M. Lengaigne, and E. Guilyardi, 2015: The impact of westerly wind bursts and ocean initial state on the development, and diversity of El Niño events. *Climate Dyn.*, **44**, 1381–1401, https://doi.org/10.1007/s00382-014-2126-4.

Gebbie, G., and E. Tziperman, 2009: Predictability of SST-modulated westerly wind bursts. *J. Climate*, **22**, 3894–3909, https://doi.org/10.1175/2009JCLI2516.1.

——, I. Eisenman, A. Wittenberg, and E. Tziperman, 2007: Modulation of westerly wind bursts by sea surface temperature: A semistochastic feedback for ENSO. *J. Atmos. Sci.*, **64**, 3281–3295, https://doi.org/10.1175/JAS4029.1.

Harrison, D. E., and P. S. Schopf, 1984: Kelvin-wave-induced anomalous advection and the onset of surface warming in El Niño events. *Mon. Wea. Rev.*, **112**, 923–933, https://doi.org/10.1175/1520-0493(1984)112<0923:KWIAAA>2.0.CO;2.

Hirst, A. C., 1986: Unstable and damped equatorial modes in simple coupled ocean–atmosphere models. *J. Atmos. Sci.*, **43**, 606–632, https://doi.org/10.1175/1520-0469(1986)043<0606:UADEMI>2.0.CO;2.

Jin, F.-F., 1997a: An equatorial ocean recharge paradigm for ENSO. Part I: Conceptual model. *J. Atmos. Sci.*, **54**, 811–829, https://doi.org/10.1175/1520-0469(1997)054<0811:AEORPF>2.0.CO;2.

——, 1997b: An equatorial ocean recharge paradigm for ENSO. Part II: A stripped-down coupled model. *J. Atmos. Sci.*, **54**, 830–847, https://doi.org/10.1175/1520-0469(1997)054<0830:AEORPF>2.0.CO;2.

——, and S.-I. An, 1999: Thermocline and zonal advective feedbacks within the equatorial ocean recharge oscillator model for ENSO. *Geophys. Res. Lett.*, **26**, 2989–2992, https://doi.org/10.1029/1999GL002297.

Kalnay, E., and Coauthors, 1996: The NCEP/NCAR 40-Year Reanalysis Project. *Bull. Amer. Meteor. Soc.*, **77**, 437–471, https://doi.org/10.1175/1520-0477(1996)077<0437:TNYRP>2.0.CO;2.

Kao, H.-Y., and J.-Y. Yu, 2009: Contrasting eastern-Pacific and central-Pacific types of ENSO. *J. Climate*, **22**, 615–632, https://doi.org/10.1175/2008JCLI2309.1.

Kessler, W. S., 2002: Is ENSO a cycle or a series of events? *Geophys. Res. Lett.*, **29**, 2125, https://doi.org/10.1029/2002GL015924.

Larkin, N. K., and D. E. Harrison, 2005: Global seasonal temperature and precipitation anomalies during El Niño autumn and winter. *Geophys. Res. Lett.*, **32**, L16705, https://doi.org/10.1029/2005GL022860.

Lau, K.-M., 1981: Oscillations in a simple equatorial climate system. *J. Atmos. Sci.*, **38**, 248–261, https://doi.org/10.1175/1520-0469(1981)038<0248:OIASEC>2.0.CO;2.

Lee, S.-K., P. N. DiNezio, E.-S. Chung, S.-W. Yeh, A. T. Wittenberg, and C. Wang, 2014: Spring persistence, transition, and resurgence of El Niño. *Geophys. Res. Lett.*, **41**, 8578–8585, https://doi.org/10.1002/2014GL062484.

Lengaigne, M., J.-P. Boulanger, C. Menkes, G. Madec, P. Delecluse, E. Guilyardi, and J. Slingo, 2003: The March 1997 westerly event and the onset of the 1997/98 El Niño: Understanding the role of the atmospheric response. *J. Climate*, **16**, 3330–3343, https://doi.org/10.1175/1520-0442(2003)016<3330:TMWWEA>2.0.CO;2.

——, E. Guilyardi, J.-P. Boulanger, C. Menkes, P. Delecluse, P. Inness, J. Cole, and J. Slingo, 2004: Triggering of El Niño by westerly wind events in a coupled general circulation model. *Climate Dyn.*, **23**, 601–620, https://doi.org/10.1007/s00382-004-0457-2.

Li, T., 1997: Phase transition of the El Niño–Southern Oscillation: A stationary SST mode. *J. Atmos. Sci.*, **54**, 2872–2887, https://doi.org/10.1175/1520-0469(1997)054<2872:PTOTEN>2.0.CO;2.

Long, B., and P. Chang, 1990: Propagation of an equatorial Kelvin wave in a varying thermocline. *J. Phys. Oceanogr.*, **20**, 1826–1841, https://doi.org/10.1175/1520-0485(1990)020<1826:POAEKW>2.0.CO;2.

McPhaden, M. J., 2004: Evolution of the 2002/03 El Niño. *Bull. Amer. Meteor. Soc.*, **85**, 677–695, https://doi.org/10.1175/BAMS-85-5-677.

——, and X. Yu, 1999: Equatorial waves and the 1997–98 El Niño. *Geophys. Res. Lett.*, **26**, 2961–2964, https://doi.org/10.1029/1999GL004901.

——, T. Lee, and D. McClurg, 2011: El Niño and its relationship to changing background conditions in the tropical Pacific Ocean. *Geophys. Res. Lett.*, **38**, L15709, https://doi.org/10.1029/2011GL048275.

Miyama, T., and T. Hasegawa, 2014: Impact of sea surface temperature on westerlies over the western Pacific warm pool: Case study of an event in 2001/02. *SOLA*, **10**, 5–9, https://doi.org/10.2151/sola.2014-002.

Perez, C. L., A. M. Moore, J. Zavaly-Garay, and R. Kleeman, 2005: A comparison of the influence of additive and multiplicative stochastic forcing on a coupled model of ENSO. *J. Climate*, **18**, 5066–5085, https://doi.org/10.1175/JCLI3596.1.

Philander, S. G. H., 1983: El Niño Southern Oscillation phenomena. *Nature*, **302**, 295–301, https://doi.org/10.1038/302295a0.

Picaut, J., F. Masia, and Y. du Penhoat, 1997: An advective-reflective conceptual model for the oscillatory nature of the ENSO. *Science*, **277**, 663–666, https://doi.org/10.1126/science.277.5326.663.

Ren, H.-L., and F.-F. Jin, 2013: Recharge oscillator mechanisms in two types of ENSO. *J. Climate*, **26**, 6506–6523, https://doi.org/10.1175/JCLI-D-12-00601.1.

Reynolds, R. W., T. M. Smith, C. Liu, D. B. Chelton, K. S. Casey, and M. G. Schlax, 2007: Daily high-resolution-blended analyses for sea surface temperature. *J. Climate*, **20**, 5473–5496, https://doi.org/10.1175/2007JCLI1824.1.

Roundy, P. E., and G. N. Kiladis, 2006: Observed relationships between oceanic Kelvin waves and atmospheric forcing. *J. Climate*, **19**, 5253–5272, https://doi.org/10.1175/JCLI3893.1.

Schopf, P. S., and M. J. Suarez, 1988: Vacillations in a coupled ocean–atmosphere model. *J. Atmos. Sci.*, **45**, 549–566, https://doi.org/10.1175/1520-0469(1988)045<0549:VIACOM>2.0.CO;2.

Seiki, A., and Y. N. Takayabu, 2007: Westerly wind bursts and their relationship with intraseasonal variations and ENSO. Part II: Energetics over the western and central Pacific. *Mon. Wea. Rev.*, **135**, 3346–3361, https://doi.org/10.1175/MWR3503.1.

Suarez, M. J., and P. S. Schopf, 1988: A delayed action oscillator for ENSO. *J. Atmos. Sci.*, **45**, 3283–3287, https://doi.org/10.1175/1520-0469(1988)045<3283:ADAOFE>2.0.CO;2.

Tseng, Y.-H., Z.-Z. Hu, R. Ding, and H.-C. Chen, 2017a: An ENSO prediction approach based on ocean conditions and ocean–atmosphere coupling. *Climate Dyn.*, **48**, 2025–2044, https://doi.org/10.1007/s00382-016-3188-2.

——, R. Ding, and X.-M. Huang, 2017b: The warm blob in the northeast Pacific—The bridge leading to the 2015/16 El Niño. *Environ. Res. Lett.*, **12**, 054019, https://doi.org/10.1088/1748-9326/aa67c3.

Tziperman, E., and L. Yu, 2007: Quantifying the dependence of westerly wind bursts on the large-scale tropical Pacific SST. *J. Climate*, **20**, 2760–2768, https://doi.org/10.1175/JCLI4138a.1.

Wyrtki, K., 1975: El Niño—The dynamic response of the equatorial Pacific Ocean to atmospheric forcing. *J. Phys. Oceanogr.*, **5**, 572–584, https://doi.org/10.1175/1520-0485(1975)005<0572:ENTDRO>2.0.CO;2.

Yu, L., R. A. Weller, and W. T. Liu, 2003: Case analysis of a role of ENSO in regulating the generation of westerly wind bursts in the western equatorial Pacific. *J. Geophys. Res.*, **108**, 3128, https://doi.org/10.1029/2002JC001498.